

# Analysis of metal-poor galaxy spectra in the redshift range 0.00574-0.05368

M. Contini<sup>1,2</sup>

<sup>1</sup> Dipartimento di Fisica e Astronomia "G. Galilei", University of Padova, Vicolo dell'Osservatorio 3, 35122 Padova, Italy

<sup>2</sup> School of Physics and Astronomy, Tel Aviv University, Tel Aviv 69978, Israel

Received

## ABSTRACT

We present an analysis of the metal-poor galaxy spectra in the redshift range  $0.00574 \leq z \leq 0.05368$  which were reported by Nakajima et al (2022) in their EMPG (extreme metal poor galaxy) sample. The models account for the active galactic nuclei (AGN) and the starburst (SB) galaxies, for accretion and ejection, for the physical parameters and the element abundances. The results are obtained in particular for the two cases, the emitting nebula is ejected outward from the galaxy radiation source (RS) and the emitting nebula is accreted towards the RS. We adopt the code `SUMA` which allows to choose the direction of the clouds relative to the RS. The modelling results which reproduce a single galaxy spectrum with the highest precision allow to classify this object as an AGN ejecting, an AGN accreting, an SB ejecting or an SB accreting type. When more models are equally valid we suggest that the galaxy is the product of merging. Our results show that among the eleven sample galaxies five are such. We focus on the N/O trends with the oxygen metallicity and with the redshift to identify the nitrogen/oxygen relative formation processes and the process-rates, respectively, for intermediate-mass stars. Our results show that O/H relative abundances calculated for the sample galaxies are lower than solar by a factor  $\leq 5$ . Yet, a few values were found above solar. He/H were calculated lower than solar by factors  $\leq 100$  and N/H by factors  $\leq 135$ .

**Key words.** radiation mechanisms: general — shock waves — ISM: O/H abundances — galaxies: starburst — galaxies: AGN — galaxies: local

## 1. Introduction

The exploration of pristine galaxies is one of the issues concerning galaxy spectral analysis in search of the Universe conditions at cosmic dawn. The first hints were obtained by the interpretation of high redshift ( $z > 6$ ) galaxy spectra when new powerful telescopes e.g. the James Webb Space Telescope (JWST) were installed (Vanzella et al 2023, Shaerer et al 2002, 2003, Erb et al 2002, etc). Low metallicity is a basic prerogative of early time galaxies. However, the data concerning the line fluxes for each of the observed objects are few and hardly constrain the results of modelling. Yet, those obtained by modelling the line spectra of low redshift galaxies by applying the direct strong line method to local young, low-mass and metal poor objects show very low element abundances. Therefore the methods adopted for the spectral analysis of high  $z$  galaxies are similar to those adopted for local objects, e.g. the strong line and the  $T_e$  one which are used to calculate metallicity in terms of the O/H relative abundance from the observed data (e.g. Berg et al 2012, Umeda et al 2022, Izotov et al 2021, etc) in search for pristine galaxy residuals. Nakajima et al (2022) claim that the direct  $T_e$  method is not always available due to the faint nature of the [OIII]4363 line. They investigate optical line metallicity indicators together with fundamental UV properties of extreme metal poor galaxies (EMPG). They explore the EMPG, in particular those with metallicity 10% solar ( $12 + \log(O/H) < 7.69$  based on Asplund et al (2009) solar composition).

In this paper we focus on the interpretation of the galaxy spectra in the local Universe sample presented by Nakajima et al (2022) in the  $0.00574 \leq z \leq 0.05368$  redshift range. This range is not more special than the others. Yet, this sample adds more data

to Contini (2022, hereafter Paper I) collection of spectra with [OIII]5007+/H $\beta$  line ratios from 3.2 to 10 and [OII]/H $\beta$  from 0.2 to 0.85 observed at low  $z$ , which are generally defined as star-forming galaxies. However, such line ratios appear also in some AGN spectra. We will use for investigating this sample spectra ejection and accretion models. This approach to the interpretation of the spectra offers a stronger constraint to model selection. In particular, we aim to compare our results with the O/H metallicities calculated by Nakajima et al who deduced that  $12 + \log(O/H)$  is within 6.9 and 8.9. We would like also to investigate the trends of the physical and chemical parameters throughout the redshift range reported by Nakajima et al. To analyse this issue the code `SUMA` which accounts for the coupled effect of photoionization and shock (Contini & Aldrovandi 1983, Viegas & Contini 1994 and references therein) is adopted. The results obtained for local galaxies by `SUMA` for a number of samples selected by Contini (2022) show O/H abundance ratios from near-solar to lower than solar by factors  $\leq 2$ . Much lower O/H were calculated for the EMPG sample by the strong line method by Nakajima et al reaching 10% of the solar value. The He/H relative abundances remained uncertain (e.g. Paper I, Dittman et al 2001, Hunger et al 1999, Do et al 2018, Isotov et al 2021). It is still an open question which needs special care therefore we will investigate the role of the weak lines e.g. HeII 4686 and [OIII]4363 in constraining the models. We suggest that by the detailed modelling of all the line ratios presented by the observations within single spectra the full picture of the physical characteristics and of the element abundances throughout the galaxy gaseous clouds can be reached. The distribution of the line ratios - observed from pristine galaxies - throughout the classification schemes (Kauffmann et al 2003, Kewley et al 2001) adopted for

**Table 1.** Selected galaxies from the Nakajima et al. (2022)

galaxy	ID	z
HSC J0845+0131	N1	0.01333
HSC J0935-0115	N3	0.01621
HSC J1237-0016	N5	0.05045
HSC J1401-0040	N6	0.01168
HSC J1407-0047	N7	0.05368
HSC J1411-0032	N8	0.02617
HSC J1452+0241	N9	0.00574
SDSS J1044+0353	N10	0.01317
SDSS J1253-0312	N11	0.02301
SDSS J1323-0312	N12	0.02275
SDSS J1418+2102	N13	0.00889

the local ones with similar spectral characteristics was also discussed by Nakajima et al (2022). This modelling method which is based on galaxy samples rich in number of objects gives results on a large scale (e.g. Berg et al 2016).

We adopt the code `SUMA` because it allows to choose the direction of the clouds relative to the RS. The results are obtained in particular for the two cases, the emitting nebula is accreted towards the RS and the emitting nebula is ejected outwards from the galaxy RS, i.e. both the photoionizing radiation flux and the shock act on the same edge of the emitting clouds or on the opposite edges, respectively, leading to different ion distribution profiles between them. The cloud motions which follow from the interaction with the interstellar medium (ISM) of star formation events relative to the RS location in the galaxy discs or in the presence of winds and jets (Sancisi et al 2008, Murray & Chang 1997, etc) result in accretion or ejection modes. Zhang et al (2023) claim that the gas is expelled from the galaxies by winds and jets and by galaxy merging processes at earlier  $z$ , while Ginolfi et al (2023) on the basis of the ALMA data discussed gas outflow for metal enriched gas and for e.g. the AGN A1689-zD1 at  $z > 7$ .

Accretion onto galaxy disc such as gas inflow from the circum galactic medium and merger events could generate large scale shocks (Goldman 2024) and turbulence in the disc outskirts (Goldman & Fleck 2023). With regards to AGN, Dittmann, Cantiello & Jermin (2021) found that tidal effects from the supermassive black hole (SMBH) significantly alter the evolution of stars in AGN discs. They claim that "in addition to depending on the ambient density and sound speed, the fate of stars in AGN discs depends sensitively on the distance to and mass of the SMBH. Not only the location in the disc in which stellar explosions occur is affected but different types of chemical enrichment take place." Moreover, there is a SMBH maximum luminosity above which the outward pressure exceeds the inward pull of gravity. Concluding, it is suggested that accretion and ejection are related to the element abundances. We will check by modelling the single spectra whether accretion or ejection are more appropriated to each galaxy of the Nakajima et al sample. The spectra presented by Nakajima et al (2022) for a sample of galaxies at  $z$  between 0.00574 and 0.05045 are modelled in Sect. 2. We will proceed by classifying the sample galaxies on the basis of the models which best reproduce the observation data. The results are discussed considering the physical and chemical parameter trends as function of  $z$  in Sect. 3. Concluding remarks follow in sect. 4.

## 2. Modelling the Nakajima et al (2022) sample

Kojima et al (2020) presented data for 10 EMPG, three of which were selected from the Subaru/Hyer Suprime-Cam (HSC) Subaru strategic Program (SSP) catalog and 7 were from the Sloan Digital Sky Survey (SDSS). Using [OIII] 4363 as electron temperature probe, the EMPRESS team confirmed 2 new EMPG including HSC J1631+4426 which shows the lowest metallicity ever reported. Nakajima et al (2022) paper is part of the EMPRESS program by Kojima et al (2020). Another spectroscopic follow-up by Isobe et al (2021) for 13 EMPG candidates all of which were HSC-selected, was performed with Keck/LRIS. In their paper Nakajima et al report the properties of nine new HSC galaxies and four SDSS (MagE sources). They obtained  $12+\log(\text{O}/\text{H})$  between 6.9 and 8.9 corresponding to  $0.02-2 Z_{\odot}$ .

The spectra presented by Nakajima et al show a number of significant lines rich enough to constrain the models. Degeneracy decreases when more lines are reported in a spectrum. There is a set of selected lines from the most significant ones (e.g. [OIII] doublet in the optical range, [OII] doublets in the optical-near-UV and optical-near-infrared, HeII, [NII],  $H\alpha$ ,  $H\beta$  and  $H\gamma$ ) which constrain the model in the optical range. In the UV the set is composed of UV lines. This argument is also connected with the choice of the grids of models (see sect. 2.1) which should be not-uniform, in the sense that in some critical ranges some grid- meshes are reduced as much as to obtain a better fit to all the observed line ratios.

In Table 1 we report the galaxies selected from Nakajima et al sample for our investigation. HSC J0912-0104 and HSC J1210-0103 were neglected because the data are not enough to constrain the models. An identification number (N1-N13) is assigned to each galaxy in Table 1 omitting N2 and N4. The results reported by Nakajima et al are calculated by radiation dominated models which reproduce the observed spectra by satisfactory precision focusing on the strong lines. The origin of a line strength can be the same for the oxygen ones as well as for the other elements. Quoting Kewley & Dopita (2002) "oxygen is used as a reference element because it is relatively abundant, it emits strong lines in the optical regime, it is observed from several ionization-level lines" and because it has a high collision strength (Osterbrock 1974). The weakest lines generally have low collision strengths (e.g. [OIII]4363), they depend strongly enough on the temperature of the emitting gas, and/or (e.g. [OII]3727+3729) they have low critical densities for collisional deexcitation.

The  $T_e$  method is adopted by the majority of the authors who calculate in particular the O/H metallicity. We intend to reproduce as close as possible all the lines (from different ions of different elements) presented by the observations in each spectrum consistently, i.e. with the same model. The shocks which are invoked to resolve the hydrodynamical picture, are included in the calculations. The set of the input parameters which leads to the most acceptable fit of the whole spectrum represents the final model. We consider that the contribution of gas in different conditions throughout the clouds downstream of the shock front should be accounted for. Here, compression can be strong and temperatures can be high depending on the shock velocities. The physical conditions can vary within a large range throughout the clouds when shocks are at work. This leads to discrepancies between the results obtained by the  $T_e$  methods compared to those obtained by our models (see e.g. Paper I). However our modelling method which selects each model through a large grid requires long time spending for each of them and it is therefore

less adapted to the huge number of galaxy spectra provided by modern surveys. The sample presented by Nakajima et al (2022) in their Table 1 is suitable to our investigation. Nakajima et al neglected AGNs in their models. We consider also AGN dominated models in the present analysis and we compare the results with those obtained for SB dominated galaxies.

### 2.1. Model calculations: the input parameters

The code *SUMA* accounts for photoionization and shock. The input parameters related with the shock are : the shock velocity  $V_s$ , the preshock density  $n_0$  and the preshock magnetic field  $B_0$ . A first hint to  $V_s$  comes from observed FWHM of the lines, e.g. [OIII]5007,4959 and for  $n_0$  it comes from the observations of the characteristic line ratios such as [SII] 6716/6730 and/or [OII]3727/3729. However, the [OII] lines are often blended and [SII] may contain a large contribution from diffuse extragalactic gas. Then, to obtain more information about the input parameters which define the model, we consult the grids calculated by Contini & Viegas (2001a,b). From these grids we can also distinguish between shock dominated models or radiation+shock coupled models. We select the initial parameter set among those which yield results as close as possible to the observation data. On this basis we start to build a grid. However, the grid- meshes for each of the physical and chemical parameters are often modified comparing the calculation results with the data until all or at least most of the line ratios in a single spectrum are successfully reproduced. The calculations combine photoionization and heating by the primary and secondary radiation fluxes with collisional ionization and heating.

For all models  $B_0=10^{-4}$ Gauss is adopted in the present work.  $V_s$  and  $n_0$  are used in the calculations of the Rankine-Hugoniot equations at the shock front and downstream. They are combined in the compression equation (Cox 1972) which is resolved throughout each slab of the gas in order to obtain the density profile downstream. This is a prerogative of models accounting for the shock. The higher  $B_0$ , the lower the compression  $n/n_0 \propto (1/B_0)$ .  $B_0$  is chosen such as to obtain the density  $n$  in the range observed in the SB and AGN emitting clouds. As  $n_0$  and  $B_0$  are correlated, the series of preshock-densities which better reproduce the spectra of the Nakajima sample galaxies corresponds to a sequence of frozen-in magnetic fields  $B = n B_0/n_0$ .

Primary radiation from the starburst is approximated by a black-body. The input parameters are the effective temperature  $T_*$  and the ionization parameter  $U$ . A pure black-body radiation referring to  $T_*$  is a poor approximation for a starburst, even adopting a dominant spectral type. We follow the Rigby & Rieke (2004) advise to adopt black body radiation for SB on the basis of a large range of ionization parameters, effective temperatures and also relative abundances of the elements. Besides the black-body spectral energy distribution (SED), we use also power-law SEDs when the radiation flux comes from an AGN. Moreover, we combine both the black-body and the power-law with collisional ionization by the shock. This paper, as well as other papers which show the results of models of shocks and photoionization, is aimed to provide an answer about the role of the shocks in the interpretation of the spectra. Comparison of the ionization rates for the primary radiation, for the secondary diffuse radiation and for collisional ionization rates for some interesting ions as function of the temperature in the gaseous clouds are shown by Contini (1997, Figs. 3-5). At  $T \sim 10^5$  K, i.e. in the UV domain, collisional ionization rates dominate.

The input parameter which represents the radiation field in AGNs is the power-law flux from the active centre (AC)  $F$  in number of photons  $\text{cm}^{-2} \text{s}^{-1} \text{eV}^{-1}$  at the Lyman limit. The spectral indices are  $\alpha_{UV}=-1.5$  and  $\alpha_X=-0.7$ .

When the primary radiation flux - which depends on the RS - reaches the clouds, it affects the surrounding gas. This region is not considered as a unique cloud, but as a sequence of slabs with different thickness calculated automatically following the temperature gradient. The secondary diffuse radiation is emitted from the slabs of gas heated by the radiation flux reaching the gas and by the shock. Primary and secondary radiations are calculated by radiation transfer through the slabs. The line fluxes which appear within the spectra are calculated integrating throughout the clouds on a maximum of 300 slabs.

The geometrical thickness of the emitting clouds  $D$  and the relative abundances of the elements to H are input parameters. In our model the line and continuum emitting regions throughout the galaxy cover an ensemble of fragmented clouds. The geometrical thickness of the clouds is calculated consistently with the physical conditions and element abundances of the emitting gas.  $D$  is hardly deduced from the observations. It determines whether the models are matter-bounded or radiation-bounded. The shocks can create turbulence directly via the Richtmyer-Meshkov instability (Meshkov 1969). In addition the shocks can generate shear flows which in turn can create turbulence by shear instability and by the Kelvin-Helmholtz instability. The turbulence is expected to be supersonic and could cause fragmentation of matter that leads to clouds with very different geometrical thickness coexisting in the same galaxy (see e.g. Fonseca-Faria et al 2023).

The abundances of the elements which enter directly in the calculation of the line intensities, affect in different ways the cooling rate of the gas downstream and consequently they shape the distribution of the ion fractional abundances throughout the clouds. They are calculated resolving in all the slabs the ionization equations for each element (H, He, C, N, O, Ne, Mg, Si, S, Ar, Cl, Fe) in each ionization level. Finally, the calculated line ratios, integrated throughout the cloud thickness, are compared with the observed ones. The calculation process is repeated changing the input parameters until the observed data are reproduced by the model results, at maximum within 10-20 percent for the strongest lines and within 50 percent for the weakest ones. Those thresholds are indicated by the approximation of the coefficients (for ionization, recombination, dielectric recombination, etc) used in model calculations and by the observation errors which can reach 50% in the weak lines flux. The accuracy of the chemical abundance determination can be reached depending on the number of meshes in the grids and their dimensions. The accuracy of the calculated coefficients which compose the code depends on quantum mechanics. A better fit of the spectra can be found by running more models and building grids with relatively small meshes.

The dust-to-gas (d/g) ratio is also an input parameter. It regards in particular the SED affecting dust reprocessed radiation and its peak. Moreover, a high d/g can reduce the non radiative to a radiative shock through the mutual collisional heating and cooling of dust grains and gas atoms.

### 2.2. Model calculations: the line ratios

The line intensities calculated in each slab of gas are integrated throughout the clouds taking into consideration the radiation flux from the RS and the shocks. We first try to reproduce the relatively high line ratios (e.g. [OIII] 5007+4959/H $\beta$ , [OII]

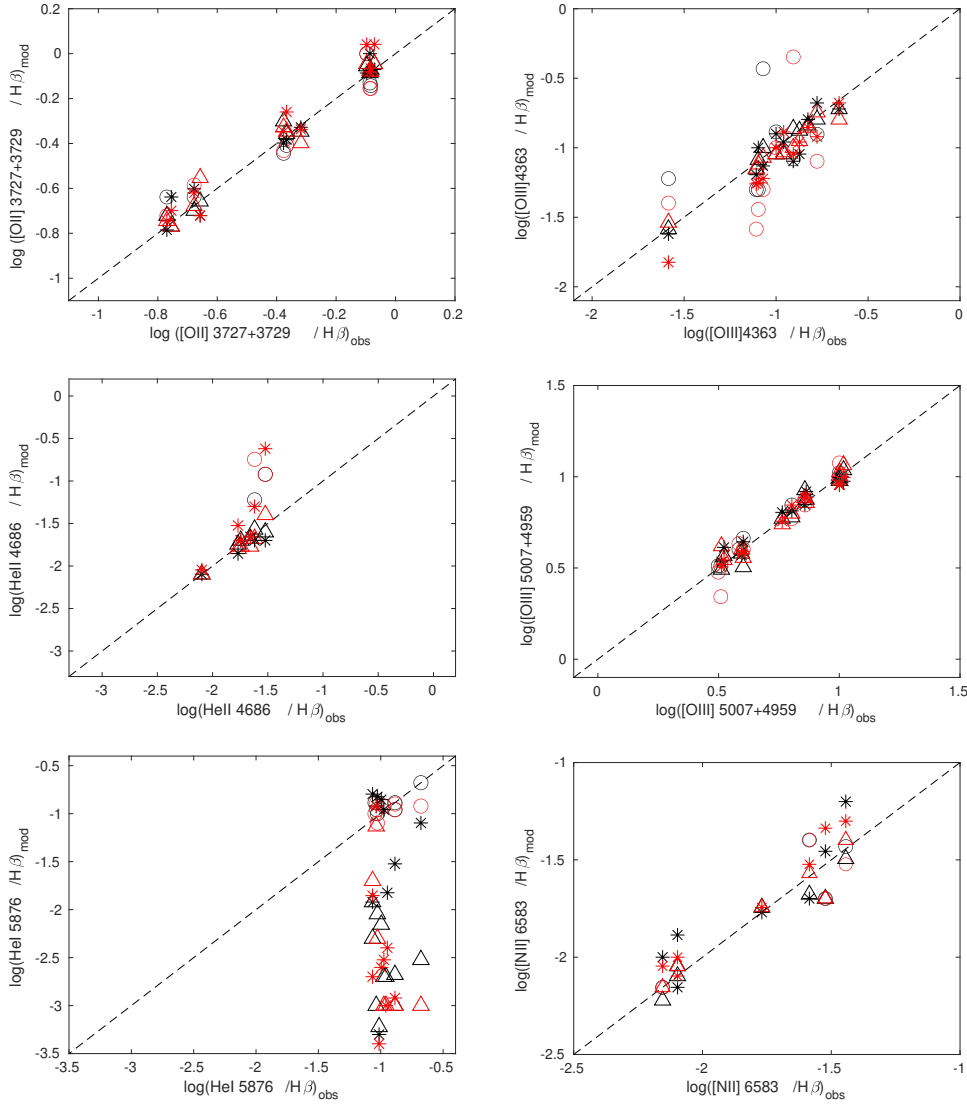


**Fig. 1.** Calculated (mod) versus observed (obs) line ratios to  $H\beta$ . Black symbols refer to accretion, red ones to ejection. Open circles: models (mp) calculated by radiation adapted to an AGN and solar He/H; open triangles: models (mh) calculated by radiation adapted to AGN and by different He/H. Asterix: models (ms) calculated by radiation adapted to starbursts and different He/H. The models are described in the bottom of Tables A.1-A.8

$3727+3729/H\beta$ ) constraining the physical parameters to best fit all the available oxygen line ratios including  $[OIII]4363/H\beta$ . The  $[NII]/H\beta$  ratios are calculated considering that charge exchange reactions are at work between  $O^+$  and  $H^+$  and between  $N^+$  and  $H^+$ . Therefore,  $[NII]/[OII]$  are adjusted by selecting the most suitable N/O relative abundance. The  $[NeIII]3689+/H\beta$  ratios (the plus indicates that the doublet is accounted for) follow the  $[OIII]5007+/H\beta$  ones due to their atomic structures. They are regulated by the Ne/H relative abundance.

The line ratios to  $H\beta=1$  are then compared with the data and the best fitting models are selected. They appear in Tables A.1-A.8. Each galaxy from the Nakajima et al sample is identified by the number which appears in Table 1. In the following  $[OIII]5007+$  indicates  $[OIII]5007+4959$ ,  $[OII]$  indicates  $[OII]3727+3729$ , HeII indicates HeII 4686,  $[NII]$  indicates  $[NII]6583$  and HeI indicates HeI 5876. In row 13 of Tables A.1-A.8 the  $H\beta$  flux calculated at the nebula is reported, followed in rows 14-18 by the values of the physical parameters adopted for each model and of the relative abundances of the elements

to H in rows 19-23. We adopt the simplified picture of a cloud moving towards the photoionizing source or in the opposite direction as accretion or ejection, respectively. The calculations translate to radiation from the RS (such as the AC for AGN) reaching the very shock front edge of the cloud (accretion) or radiation reaching the edge opposite to the shock front (ejection). We will calculate the line ratios in both cases and we will try to reproduce the observed ones. Each galaxy spectrum presented in Tables A.1-A.8 therefore is splitted into accretion and ejection identified by the parameters  $str=0$  and  $str=1$ , respectively, which appear in the bottom row.

In particular, in Tables A.1-A.2 the observed line ratios are compared with model results mp1.0 - mp9.0 and mp1.1 - mp9.1 (recall that 0 refers to accretion and 1 to ejection). The models account for the radiation flux from the AC adapted to an AGN i.e. a power-law and solar He/H. The other element ratios to  $H\beta$  are selected among the best fitting ones. In Tables A.3-A.5 the observation data are compared with models mh1.0-mh13.0 and mh1.1-mh13.1 obtained adopting a power-law flux

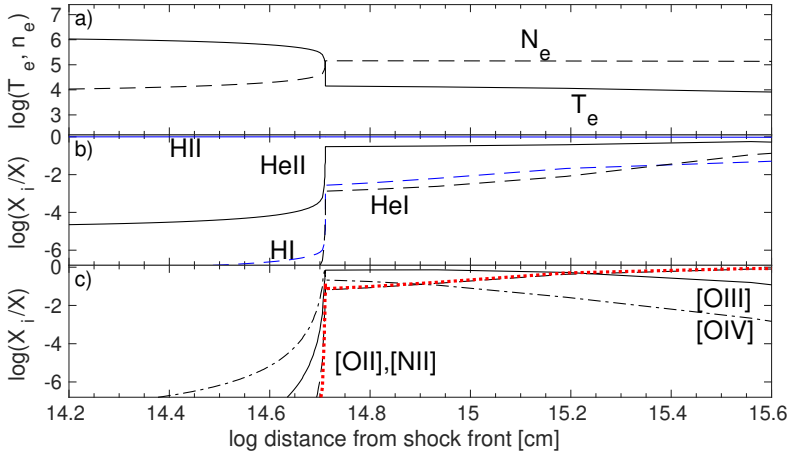


**Fig. 2.** Profiles of the physical parameters throughout the N12 galaxy clouds in the accretion case: the shock front and the edge reached by the AC flux are both on the left. Top diagram: black lines:  $T_e$  (solid),  $N_e$  (dashed); middle diagram: blue: HI (dashed), HII (solid); black : HeI (dashed), HeII (solid); bottom diagram: black lines refer to oxygen ionization stages: [OIV] (dot-dashed), [OIII] (solid), [OII] (dashed); red dotted line: [NII]

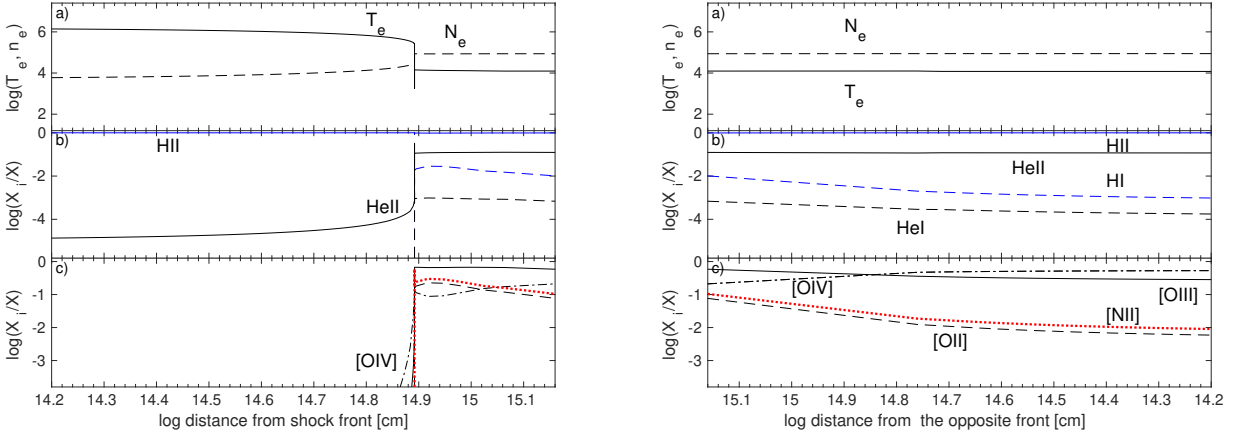


**Fig. 3.** The ejection case. The clouds are divided in two contiguous halves which are displayed by the left and right panels. In the left panel the shock front is on the left and the X-axis scale is logarithmic. In the right panel the right edge is reached by the flux from the AC. The X-axis scale is logarithmic in reverse in order to have the same detailed view of the cloud edges. Symbols as in Fig.2.

as for AGN and the He/H relative abundances best fitting the observed HeII4686/H $\beta$  line ratios. In Tables A.6-A.8 the data are compared with models ms1.0-ms13.0 and ms1.1-ms13.1 obtained adopting a black body radiation flux as that used for starbursts (see Paper I) and consistent He/H.

Fig. 1 confirms in a graphical way the results presented in Tables A.1-A.8. We neglected the data error bars both to obtain a clear picture and to easily distinguish the less fitting results. Fig. 1 shows that the error is minimum for [OIII]5007+ /H $\beta$ , increasing for [OII]/H $\beta$  ratios which are low in the present galaxy sample. Discrepancies can be high for [OIII]4363/H $\beta$  ratios which are even lower than [OII]/H $\beta$ .

O/H was found underabundant by a factor  $\leq 5$  relative to solar ( $(O/H)_\odot = 4.9 \times 10^{-4}$ , Grevesse 2019) in mh1.1 in N1 and mh3.1 in N3 and higher than solar in AGN mh13.1, mh10.1 and in both SB and AGN N3, N11 and N8 (see Table 4.) Ne/H relative abundances are lower than solar by 40% ( $(Ne/H)_\odot = 8.5 \times 10^{-5}$ , Grevesse 2019, Young 2018). About [SII]6716/H $\beta$  and [SII]6730/H $\beta$ , the observed [SII]6717/[SII]6730 (see Tables A.1-A.8) doublet line ratios are

generally  $\geq 1$  indicating very low electron densities (Osterbrock 1974) which are less suitable to galactic clouds. The disagreement with model results which show ratios  $< 1$  is explained by the contribution of diffuse intergalactic gas (Paper I). In fact, the first ionization potential of S is 10.31 eV, lower than that of H (13.51 eV) and the [SII] lines can be strong in the ISM where temperatures and densities are relatively low ( $T \leq 10^4$ K,  $n_0 < 10$  cm $^{-3}$ ). The hydrogen line ratios H $\alpha$ /H $\beta$  and H $\gamma$ /H $\beta$  are calculated in each slab. H $\gamma$ 4340 can be blended with [OIII]4363 and H $\alpha$  is blended with the [NII]6548, 6583 doublet. H $\alpha$ /H $\beta$  ratios are used to correct the spectra from reddening. The values are generally fixed to  $\leq 3$  considering  $T \leq 10^4$ K. However models accounting for the shocks lead to large regions of gas at higher temperatures therefore model results show also H $\alpha$ /H $\beta$   $\geq 3$ .

### 2.2.1. Helium lines

We focus on the He lines following the results discussed in Paper I. In Nakajima et al (2022, their table 1) HeII 4686/H $\beta$  lines are weak compared to those in AGN spectra which can be

strong (Aldrovandi & Contini 1985). The HeI 5876 lines on the other hand are  $\sim 0.1$  in the spectra from different objects. The HeII/H $\beta$  ratios in the N1, N5 and N9 spectra are upper limits and in N7 and N8 are not provided by the data. We adopted solar He/H in the first modelling trial of HSC galaxies (N1-N9) because it generally fits the HeII/H $\beta$  and HeI/H $\beta$  line ratios observed from various objects at different redshifts (Tables A.1 and A.2). We realized that solar He/H ((He/H) $_{\odot}$  = 0.085 from Grevesse 2019) was too high and that for nearly all the objects the HeII/H $\beta$  line ratios calculated by models mp1.0 - mp9.0 and mp1.1 - mp9.1 overpredicted at least by a factor of 10 the observed values, while the calculated HeI 5876/H $\beta$  line ratios nicely reproduced the data. Therefore, we repeated the modelling of the spectra of all the galaxies by more adapted He/H relative abundances by models mh1.0-mh13.0, mh1.1-mh13.1, ms1.0-ms13.0 and ms1.1-ms13.1 (Tables A.3 - A.8).

HeII/H $\beta$  line ratios in the spectra reported by Nakajima et al are reproduced by AGN dominated models with He/H lower than solar by factors between  $\sim 100$  for mh12.1 and 1.7 for mh7.1 (Tables A.3-A.5). Solar and higher than solar He/H were certainly not found for some galaxies spectra where the observed HeII/H $\beta$  were low or absent. Moreover, low HeII/H $\beta$  line ratios cannot result from models which adopt the relatively strong radiation flux which yields [OIII]/[OII] ratios ranging between  $\sim 5$  and  $\sim 60$ . Therefore the parameter which can reduce strongly the HeII line intensity is the He abundance. We had to recalculate all the other spectral line ratios in order to reproduce the observed values because He is a strong coolant. However, the satisfactory fit found for HeI 5876/H $\beta$  for nearly all the spectra by the mp1-mp9 models (Tables A1-A2) was lost. This can be seen in Fig. 1 where we compare the observed with the calculated line ratios. The dilemma between an acceptable HeII 4686/H $\beta$  or an acceptable HeI 5876/H $\beta$  was resolved by arguing that HeI is a permitted recombination line therefore the contribution from the ISM to the observed line is sensible. This hypothesis is strengthened by the fact that HeI/H $\beta$  ratios vary within a small range (Fig. 1, left bottom diagram) in galaxies with different spectra because the diffuse ISM has temperatures  $T \leq 10^4$ K. Therefore, in the following we will adopt reduced or enhanced He/H relative abundances in order to reproduce the HeII4686/H $\beta$  line ratios neglecting the HeI/H $\beta$  fit for both AGN and SB models. The results of HSC spectra reported in Tables A.1-A.2 are constraining enough to support this discussion and the SSDS spectra will be properly calculated. The results are reported in Tables A.3-A.8.

Model results for SB galaxies appear in Tables A.6-A.8. They show that the minimum He/H results by a factor of 85 lower than solar for both ms12.1 and ms12.0 models. He/H is solar for model ms6.0 but this model does not reproduce satisfactorily the HeII/H $\beta$  line ratio. A good fit of both HeII/H $\beta$  and HeI/H $\beta$  is obtained by model ms13.0 with He/H = 0.09, but only in the accretion case. A higher than solar He/H by factors of  $\sim 3$  and  $\sim 10$  reproduces reasonably the HeII/H $\beta$  line ratios in the ms11.0 and ms6.1 spectra, respectively, but HeI 5876/H $\beta$  line ratios result overpredicted by the same factors.

Energy loss by line emission affects the cooling rate of the gas downstream, therefore changing the element abundances the physical parameter sets require remodelling. Low abundances, in particular for He which is generally a strong coolant lead to a reduced cooling rate and affect all the calculated line ratios in different ways. For the Nakajima et al spectra however we found that He is often so underabundant that increasing or decreasing He/H by factors  $\leq 10$  will not alterate the line ratios from the

other elements. As a consequence HeII/H $\beta$  ratios can be readjusted simply by modifying He/H.

## 2.2.2. Nitrogen lines

The same arguments as those adopted for HeII/H $\beta$  can be adapted to [NII]/H $\beta$  because N/H relative abundances were also found lower than solar ((N/H) $_{\odot}$  =  $6.76 \times 10^{-5}$  Grevesse 2019) by factors  $>10$ . A perfect fit of the [NII]6583/H $\beta$  line ratios is meaningless because the [NII] lines are extracted from the [NII] doublet 6583, 6548. They can be blended at high velocities and they are generally blended with the H $\alpha$  line for  $V_s$  adapted to the AGN NLR and the SB. The line ratios depend on the electron temperature and density that are not constant throughout the emitting clouds when shocks are at work. Therefore the error can be sound. [NII]/H $\beta$  line ratios in all the present observed spectra are low relative to those shown in other galaxy samples at different  $z$ . If this depends from a low nitrogen abundance, as we have explained for He, N will end its role as a strong coolant in the downstream region. Consequently, N/H will directly result by reproducing the observed [NII]/H $\beta$  line ratios.

## 2.3. Distribution of $T_e$ , $N_e$ and of oxygen ion fractional abundances downstream

The line ratios within each spectrum can be understood following the profiles of the physical parameters throughout the clouds. We present for instance in Fig. 2 and Fig. 3 the profiles of  $T_e$ ,  $N_e$  and of the main ion fractional abundances in the N12 galaxy clouds for accretion and ejection models, respectively, relative to an AGN. In models which account for the shock, immediately behind the shock front, the gas is thermalized to a temperature  $T = 1.5 \times 10^5 (V_s / [100 \text{ km s}^{-1}])^2$  K. At high temperatures e.g. for  $V_s = 300 \text{ km s}^{-1}$   $T \geq 10^6$  K, recombination coefficients are very low and the cooling rate of the gas is low. At  $T$  between  $10^4$  K and  $10^5$  K UV lines and coronal lines in the IR are strong and lead to rapid cooling and compression of the gas. If the cooling rate is so high as to drastically reduce the temperature eluding intermediate ionization-level lines, the calculated spectra will be less adapted to reproduce the observed ones because intermediate ionization-level lines (e.g. [OIII], [OII] etc) will be very weak. However, the temperature after the drop is maintained at  $10^4$ K by secondary diffuse radiation which comes from the slabs of gas heated by the shock and by the photoionizing flux. At  $T \sim 10^4$ K the gas (in particular oxygen) shows strong lines from the intermediate-ionization levels. It can be noticed that the models are matter-bounded, as it is the case for most of the galaxies where  $D$  is small ( $< 0.01$  parsec). Fig. 2 and Fig. 3 show that HeI lines are very weak. and some other recombination lines disappear. We have added in the figures the fractional abundance of  $O^{3+}/O$  although [OIV] lines were not observed by Nakajima et al to show the region of hot gas downstream where high-ionization-level lines up to e.g. the Fe coronal ones can be strong. The two phase regime which appears in Figs. 2 and 3 explains the observed spectra containing both relatively strong high ionization-level lines and the usually strong intermediate-level optical lines emitted from specific locations in a galaxy (e.g. Fonseca-Faria et al 2023).

## 3. Results

In previous sections we have found that spectra as those presented by Nakajima et al, i.e. showing [OIII]5007+/[OII]3727+

>4.8, [OIII]4363/H $\beta$  between 0.08 and 0.16 and HeII/H $\beta$  between 0.008 and 0.03, can be reproduced by strong photoionizing fluxes with a maximum of  $2.2 \times 10^{12}$  photons  $\text{cm}^{-2} \text{s}^{-1} \text{eV}^{-1}$  at the Lyman limit as for the AGN model mh5.1 (Table A.3) and a maximum  $U=0.6$  as for the SB model ms12.1 (Table A.8) and a maximum  $T_* = 180000$  K as for the SB model ms11.1 (Table A.8). Moreover, relatively low O/H with a minimum of 0.0001 by number ( $12 + \log(\text{O}/\text{H}) = 8.0$ ) as for the AGN model mh1.1 (Table A.3) and a minimum of 8.36 as for the SB model ms12.0 (Table A.8) derived from the calculations. In general, low He/H with a minimum of 0.0008 by number for the AGN model mh12.1 (Table A.5) and a minimum of 0.001 by number for the SB model ms12 (Table A.8) both accretion and ejection resulted by modelling the spectra. Upper limits were also used to constrain the models. For all the sample galaxies shock velocities similar to those which characterise the narrow line region (NLR) of Seyfert 2 galaxies ( $V_s = 100\text{-}360 \text{ km s}^{-1}$ ) and also to those ( $V_s = 160\text{-}440 \text{ km s}^{-1}$ ) used to model SB galaxies at low  $z$  (Paper I) were revealed. The calculated preshock densities were found relatively high with a peak of  $4000 \text{ cm}^{-3}$  for the AGN model mh3.0 (Table A.3) and of  $3200 \text{ cm}^{-3}$  for SB ms12.1 (Table A.8) in order to keep the [OII]/H $\beta$  line ratios low enough. The [OII] lines have critical densities for deexcitation ( $N_{e \text{ cr}} < 1000 \text{ cm}^{-3}$ ) lower than for the [OIII] lines ( $N_{e \text{ cr}} \sim 3 \times 10^5 \text{ cm}^{-3}$ ). However, for N5, N7, N8, N11, N12 AGN ejection models the densities are similar to those of Seyfert 2 galaxies. In the accretion case we can accept high preshock densities because the shock front reaches the inner regions of the NLR at a relatively small distance from the AC confirming that the density trend decreases outwards throughout the NLR. Moreover high densities downstream within the emitting clouds yield the sharp temperature drop to  $T \leq 10^4 \text{ K}$  which is followed by gas recombination to intermediate-ionization levels. They are adapted to the [OII], [OIII], [NII], [NeIII] etc line emission.

### 3.1. Selecting the galaxy types

In this work, besides the identification of each object as an AGN or as a SB, we also distinguish between accretion and ejection by considering the best approximation (in terms of the least error) in reproducing the observed line ratios. The most significant lines are employed. Model results are compared with the data which are reported in Tables A.3-A.8 for AGN accretion, AGN ejection, SB accretion and SB ejection. The same results are illustrated in Figs. 4-7. The data and model results for AGN models are shown in the top diagrams of each figure and SB models in the bottom ones. The accretion models appear in the diagrams on the left and the ejection models in the diagrams on the right. We select the best fitting model for each galaxy by neglecting high discrepancies from the data (Tables A.3-A.8). We can have a first hint from Figs. 4-6 diagrams which, however, have different axis-scales and can give only gross estimations.

In Figs. 4 and 5 diagrams the calculated and observed line ratios are compared. We consider only those involving oxygen lines to H $\beta$  (i.e. [OIII]4363/H $\beta$  versus (hereafter vs) [OIII]5007+/H $\beta$  and [OIII]4363/H $\beta$  vs [OII]3727+/H $\beta$ ) for single galaxies, respectively. The [OIII]5007+/H $\beta$  vs [OII]/H $\beta$  diagrams are omitted because all the models reproduce the line ratios within 10% for each spectrum and therefore they are not constraining. In Figs. 6 and 7 diagrams we consider line ratios to H $\beta$  from different elements, [NII]/H $\beta$  vs [OII]/H $\beta$  and [OIII]5007+/H $\beta$  vs HeII/H $\beta$ , respectively. [NII] and [OII] lines are linked by charge exchange reactions (see Figs 2 and 3) therefore N/H and O/H relative abundances play an important

**Table 2.** Classification of the sample galaxies

galaxy	type	model	H $\beta_{calc}$ <sup>1</sup>
N1	AGN	ejec	0.005
N3	AGN	accr	1.8
N5	SB	accr	0.09
N6	AGN	accr	0.06
N7	SB	ejec	0.5
N8a	AGN	ejec	1.75
N8b	SB	accr	0.156
N9	AGN	ejec	0.37
N10a	AGN	accr	0.43
N10b	SB	ejec	6.2
N11a	AGN	accr	1.33
N11b	SB	accr	0.13
N12a	AGN	accr	0.71
N12b	SB	ejec	7.1
N13a	AGN	accr	0.34
N13b	AGN	ejec	0.37
N13c	SB	ejec	4.0

<sup>1</sup> in  $\text{erg cm}^{-2} \text{s}^{-1}$ , calculated at the nebula (Tables A.3-A.8)

role in determining the relative line intensities. The scattering of the galaxies in Fig. 6, however, shows that the observation and the model trends are dictated also by the physical parameters. Another interesting trend is that of [OIII]5007+/H $\beta$  vs HeII/H $\beta$  in Fig. 7 diagrams which is well defined even by a few objects i.e. eliminating from the figure HeII/H $\beta$  upper limits (for N1, N5 and N9) and the galaxies where the line ratios were not provided by the observations (N7 and N8). Fig. 7 diagrams show that [OIII]5007+/H $\beta$  decreases as HeII/H $\beta$  increases. In AGN galaxies the [OIII]5007+4959 doublet is generally the strongest one in the optical range (see e.g. Dors et al 2021). The [OIII] doublet as well as HeII which is a relatively strong permitted line depend on the radiation flux from the AC and on the temperature of the emitting gas. This is not the case for the present sample of galaxies which show sometimes low or even absent HeII/H $\beta$  line ratios (see Paper I). The modelling of these line ratios is problematic because the behaviour of He lines as coolants of the gas throughout the clouds is less important due to their low abundance, at least by factors of 10, and can change the relative extent of the He<sup>+</sup> ion domains throughout the emitting clouds (Figs. 2 and 3). Therefore, the HeII/H $\beta$  line ratios are often unpredictable (Umeda, 2022).

### 3.2. Classification of the sample galaxies

In Table 2 we present the classification of the spectra which results from our modelling method. The data were provided by Nakajima et al. The models were selected adopting AGN, SB, accretion and ejection models. For all the SDSS galaxies (N10-N13) and for HSC N8 we found that both an AGN and an SB model are valid and can contribute to the spectrum. The galaxies showing a double or even a higher number of radiation sources are generally the product of merging (Contini 2012, 2013). The types selected by our models are only a first trial because, whichever method is adopted by the calculations, it leads to approximated results. The main cause is due to the adopted coefficient exactness and also to the observed line types in each spectrum which do not cover the whole ionization stages and therefore do not strongly constrain the models.

Tables A.3-A.8 and Figs. 4-7 suggest that:

N1 is an ejecting AGN because [OIII]4363/H $\beta$  and [OII]/H $\beta$  ratios are best fitting the data. N1 SB ejection model

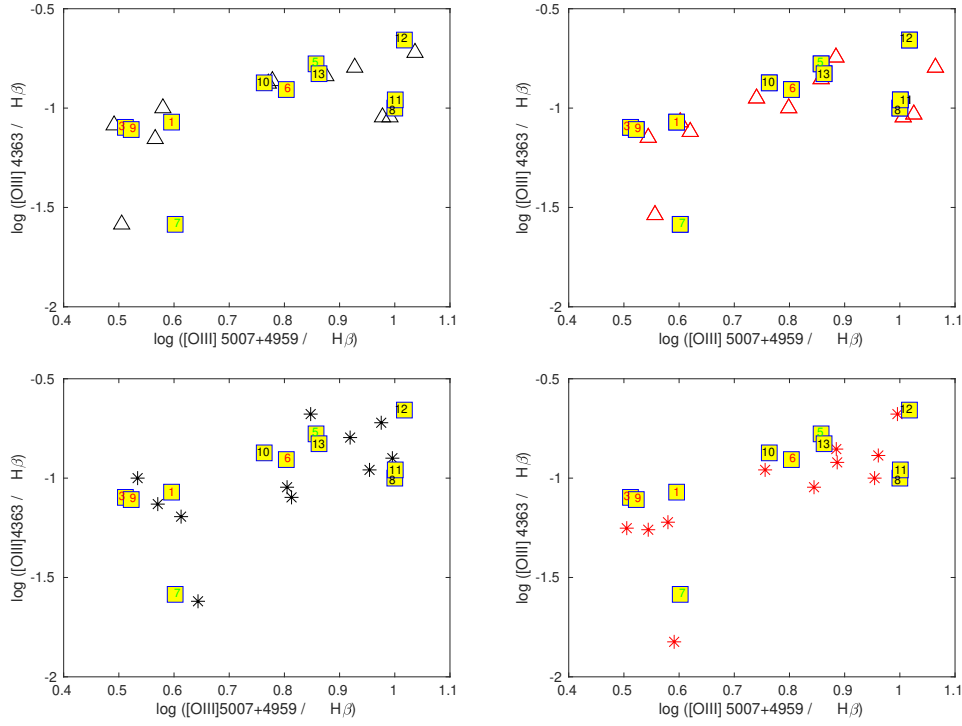


**Fig. 4.**  $[\text{OIII}]4363/\text{H}\beta$  versus  $[\text{OIII}]5007+4959/\text{H}\beta$ . Yellow filled squares represent the observed values. Other symbols as in Fig. 1 Red numbers: AGN; green numbers: SB; black numbers: merging galaxies (see sect. 3.2).

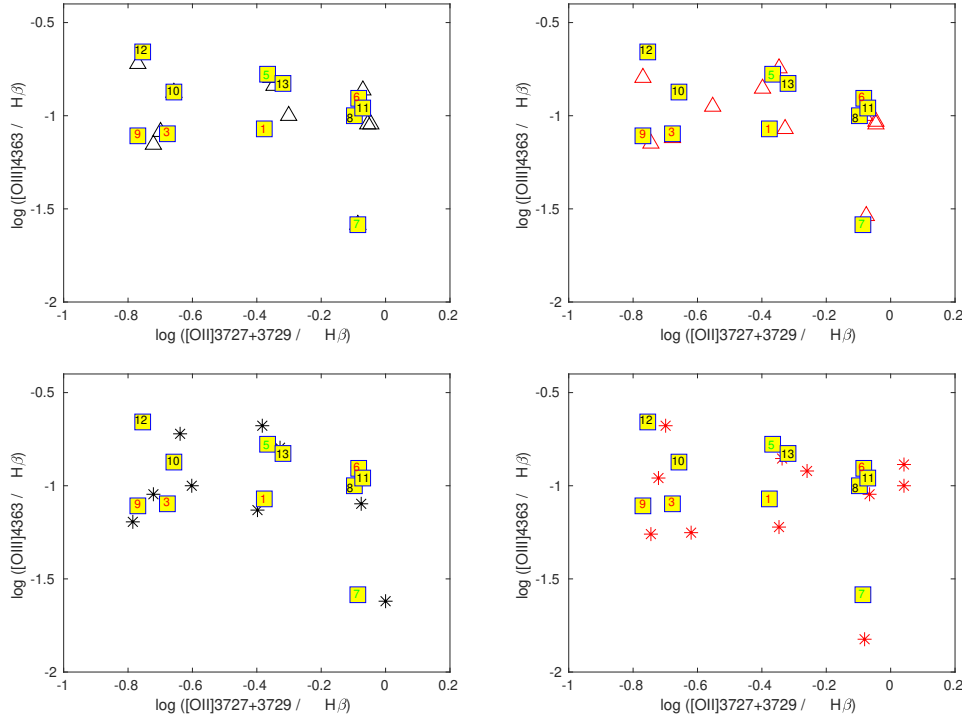


**Fig. 5.**  $[\text{OIII}]4363/\text{H}\beta$  versus  $[\text{OII}]3727+3729/\text{H}\beta$ . Symbols as in Fig. 4

should be eliminated because  $[\text{OIII}]4363/\text{H}\beta$  is underpredicted by an error of 29 % and  $\text{HeII}/\text{H}\beta$  reproduces the observed upper limit instead of underpredicting it. The SB accretion model for  $[\text{OIII}]5007+/\text{H}\beta$  corresponds to an error of 5.6 % while the error for AGN ejection is 1.5 %. Then, AGN ejection is selected for the N1 galaxy but SB accretion could contribute to some of the lines.

N3 is an accreting AGN because ejection has an  $[\text{OIII}]5007+/\text{H}\beta$  error of 28% while accretion of 4.6% and an error of 2.5 % for  $[\text{OIII}]4363/\text{H}\beta$  accretion and of 5% for  $[\text{OIII}]4363/\text{H}\beta$  ejection. The best fitting SB model has an  $[\text{OIII}]4363/\text{H}\beta$  error of 25% for accretion and of 30 % for ejection, an error of 5.5% for  $[\text{OIII}]5007+/\text{H}\beta$  accretion and of 1.5% for ejection. An error of 100% for  $\text{HeII}/\text{H}\beta$  SB ejection elimi-

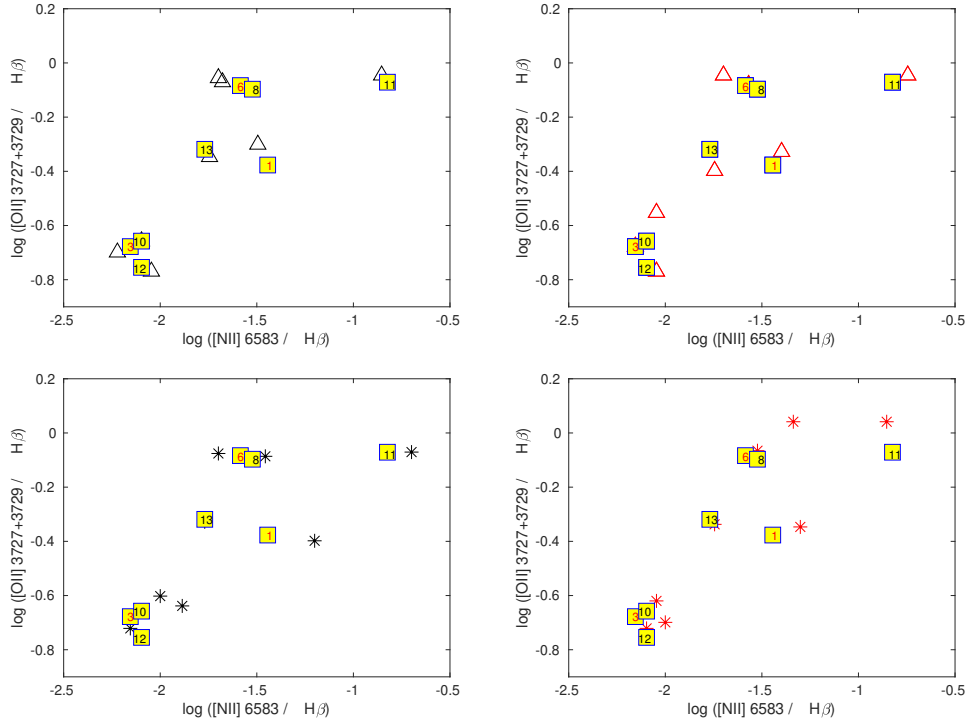


**Fig. 6.** [OII]/H $\beta$  versus [NII]/H $\beta$ . Symbols as in Fig. 2

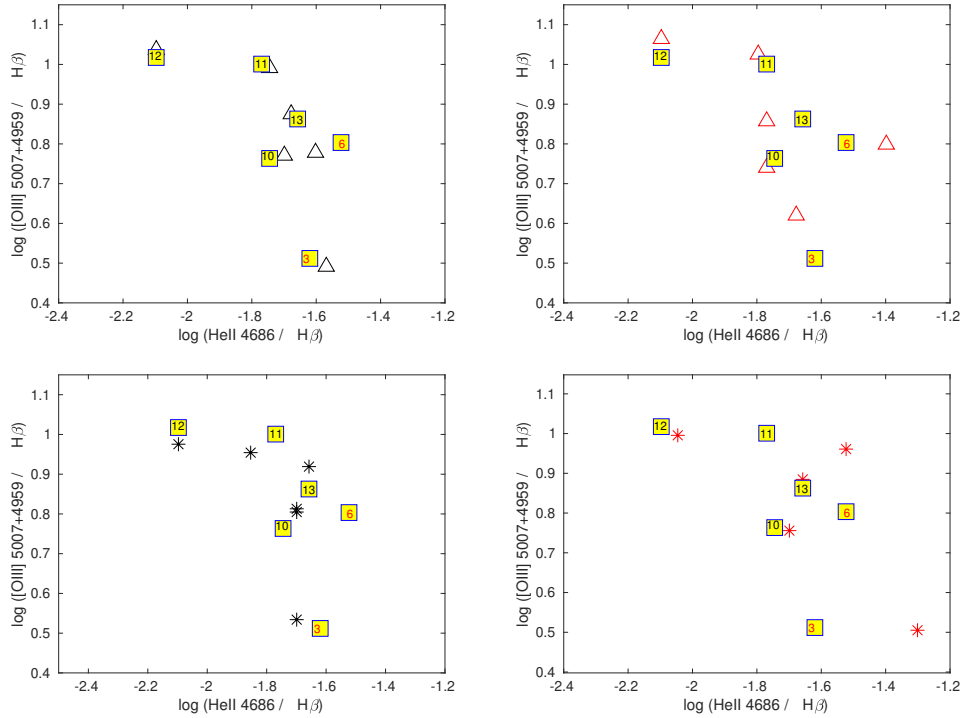


**Fig. 7.** [OIII]5007+4959/H $\beta$  versus HeII4686/H $\beta$ . Symbols as in Fig. 2

nates this model. An error of 43% for [NII]/H $\beta$  for SB accretion is also rather high. Therefore we tend to select the AGN accretion model for N3.

N5 AGN accretion shows an error of 17.5% for [OIII]5007+/H $\beta$  and of 6.3% for ejection, while N5 SB 2.2% and 6.9 %, respectively. HeII/H $\beta$  eliminates AGN ejection because it overpredicts the upper limit. The error of SB [OII]/H $\beta$  is 28% for ejection while of 3.7 % for accretion eliminating N5 SB

ejection. The errors for AGN [OII]/H $\beta$  are within 4.7. Therefore we select SB accretion for N5.

N6 AGN [OIII]4363/H $\beta$  shows errors of 10 % and 20 % for accretion and ejection, respectively. All the other lines well fit the data. For SB models the [OIII]4363/H $\beta$  ratios have errors of 48 % and 27 % , respectively. The worst fit is for SB accretion HeII/H $\beta$  with an error of 93 %. Therefore we select the AGN accretion model to represent N6 and we less recom-

mend the SB ejection model which shows an error of 10% for the  $[\text{OIII}]5007+\text{H}\beta$  line ratio.

N7 spectrum constrains the models because  $[\text{OIII}]4363/\text{H}\beta$  is an upper limit, therefore the only fitting model is for an ejecting SB (see Fig. 4).

N8 can be selected as an ejecting AGN although the error of 12.5% for  $[\text{OII}]/\text{H}\beta$  ejection is higher than for accretion (10%) but  $[\text{OIII}]5007+$  reproduces better the observed line for ejection. The eventual SB model suggests accretion.

N9 spectrum has been reproduced by good precision for the AGN  $[\text{OIII}]5007+\text{H}\beta$  and  $[\text{OIII}]4363/\text{H}\beta$  ratios in the ejection case, however, the  $\text{H}\alpha/\text{H}\beta$  ratio has an error of 56%. Therefore the accretion model is selected. From this model we obtain that the  $[\text{NII}]/[\text{OII}]$  ratio is  $\log(0.047)=-1.33$  and we can find the  $[\text{NII}]/\text{H}\beta$  true value neglecting the upper limit of 0.009. As for the SB models, we hardly select accretion due to a 23% error for  $[\text{OIII}]5007+\text{H}\beta$  and of 98% for HeII.

N10 seems definitively an accreting AGN. However an ejecting SB can be accepted as a secondary component with an error of 13.6% for  $[\text{OII}]/\text{H}\beta$  and of 18% for  $[\text{OIII}]4363/\text{H}\beta$ . AGN and SB can coexist in the same galaxy which results from merging. The SB does not need to be central and an AGN can be displaced from the central zone (Contini 2012).

N11 spectrum is well reproduced by both AGN and SB accretion models even with an error of 10% for the SB  $[\text{OIII}]5007+\text{H}\beta$  and of 18% for AGN  $[\text{OIII}]4363/\text{H}\beta$ .

N12 spectrum is well reproduced by an accreting AGN with an error of 13.6% for  $[\text{OIII}]4363/\text{H}\beta$  and by an ejecting SB with an error of 13.6% for  $[\text{OII}]/\text{H}\beta$  which is as weak as  $[\text{OIII}]4363/\text{H}\beta$ . Both can be adopted for N12 which is perhaps a merging product.

N13 spectrum is well fitted by both accretion and ejection AGN models and by an ejecting SB because the accretion  $[\text{OIII}]5007+\text{H}\beta$  line ratio shows an error of 13.8%.

### 3.3. Calculated parameter trends with $z$

Nakajima et al assumed SB models for all the galaxies. To complete the investigation we report in Fig. 8 the results for the sample objects, adopting both AGN and SB accreting and ejecting models. They are presented as function of the redshift. The calculated parameters were selected by reproducing the data within errors  $< 20\%$  for the strong lines and  $< 50\%$  for the weak ones. Our aim is to compare O/H metallicity with Nakajima et al results and to complete the modelling for each galaxy. In Fig. 8 (panels at the left) the yellow circles refer to SB accretion and the white squares to SB ejection. In the panels at the right the green circles refer to AGN accretion and white squares to AGN ejection. The redshift range is relatively small and it is included within the local universe. Therefore we wonder if extrapolating towards higher  $z$  could make sense. The number of the sample galaxies is also small, anyhow some interesting trends can be noticed.

Fig. 8 top panel is dedicated to the shock velocities ( $V_s$  in  $\text{km s}^{-1}$ ), the preshock densities ( $n_0$  in  $\text{cm}^{-3}$ ) and to the cloud geometrical thickness ( $D$  in pc). Only  $V_s$  are reported on a linear scale (not logarithmic as for the other parameters) because they range between  $100 \text{ km s}^{-1}$  and  $500 \text{ km s}^{-1}$ . Moreover, they are always referred to in these unities. Shock velocities are similar to those in the NLR of AGN. Notice the decreasing trend of  $V_s$  in AGN models with increasing  $z$  and the increasing  $n_0$  in agreement with the Rankine-Hugoniot law for the conservation of mass. This evidence suggests that the shock velocity is a prime parameter in the interpretation of AGN spectra. However,

this result characterizes only the AGN models because it seems that  $V_s$  in the SB model trend more likely increases with  $z$  while  $n_0$  remains constant. The pre-shock densities are low in the AGN ejection case because the jets collide with the ISM clouds. Ejection models for N9, N10 and N13 characterized by the highest  $V_s$  overcome the other galaxies not only regarding both AGN and SB  $V_s$  but also for the AGN geometrical thickness of the ejecting clouds and for the AGN O/H and Ne/H relative abundances (middle diagrams). The results show that the clouds are highly fragmented by turbulence near the shock front for both SB and AGN.  $D$  ranges within  $10^{-4}$  pc and  $10^{-3}$  pc for AGN, except for N9, N10 and N13 with  $D > 0.1$  pc. For SB models the  $D$  range is similar ( $10^{-2}$ - $10^{-4}$  pc) except for galaxy N1 with  $D \sim 3$  pc. N1 also corresponds to an overwhelming ionization parameter  $U$  (left bottom panel) which keeps the cloud gas ionized up to a large distance from the impinging edge.

The photoionizing flux and star temperatures are also prevailing in N9, N10 and N13 ejection models for SB galaxies (left bottom panel). Also the AC flux in AGN ejection models (right bottom diagram) is slightly higher than that calculated by accretion for the same galaxies. These arguments are valid only for galaxies at redshift  $< 0.013$ . These parameters are closer to those calculated for AGN at higher  $z$ . In the bottom left panel SB models clearly show that  $U$  and  $T$  are higher for ejection than for accretion and both slightly decrease towards higher  $z$ . Except for N6 which shows a very low temperature (bottom diagram) the ejecting clouds within SB galaxies are warmer than the accreting ones. It seems that the ejected matter is heated by a higher ionizing radiation flux which derives from stars close to outbursts while in the accretion case the stars are in a more quiescent phase.

In the middle left panel the relatively high He/H ratio for most of the SB accretion models stands out because close to solar. The same occurs for a few accretion models which show O/H solar abundances for SB (N6, N10, N8 and N5). N12 and N7 are approximated. AGN models overcome the O/H solar abundance for both accretion and ejection in N13, in N10 ejection and in N3, N11 and N8 accretion.

### 3.4. Significant line ratios

#### 3.4.1. $R_{[\text{OIII}]}$

In Fig. 9 the observed  $[\text{OIII}]5007+4959/[\text{OIII}]4363$  ( $=R_{[\text{OIII}]}$ ) line ratios are reported as function of the redshift for the sample galaxies. Special attention is given to  $R_{[\text{OIII}]}$  because we learned during the spectral fitting process that the  $[\text{OIII}]4363/\text{H}\beta$  line ratio constrains significantly the models.  $R_{[\text{OIII}]}$  does not directly depend on the O/H relative abundance, therefore we shall look for the physical parameters responsible for the different trends. Most of the galaxies show  $R_{[\text{OIII}]}$  between 40 and 50. N7 (upper limit), N8 and N11 are outstanding. All of them correspond to  $[\text{OII}]/\text{H}\beta \sim 0.8$ . Then we can include in this series also N6. It is clear that these galaxies show an increasing trend of  $R_{[\text{OIII}]}$  with  $z$ , different from the other galaxies of the sample which are nearly constant. The galaxy series are distributed following the shock velocities which determine the temperature of the gas downstream. At higher velocities the temperature of the gas emitting the  $[\text{OIII}]4363$  line strongly increases reducing the  $R_{[\text{OIII}]}$  ratio. The scattering of the data shows that also the gas density and the photoionizing flux intensity are acting. Another series of galaxies (N5, N12 and N13) in the present sample includes those characterized by a strong flux  $\geq 10^{12}$  photons  $\text{cm}^{-2}$   $\text{sec}^{-1}$  eV $^{-1}$  at the Lyman limit, in the ejection case.

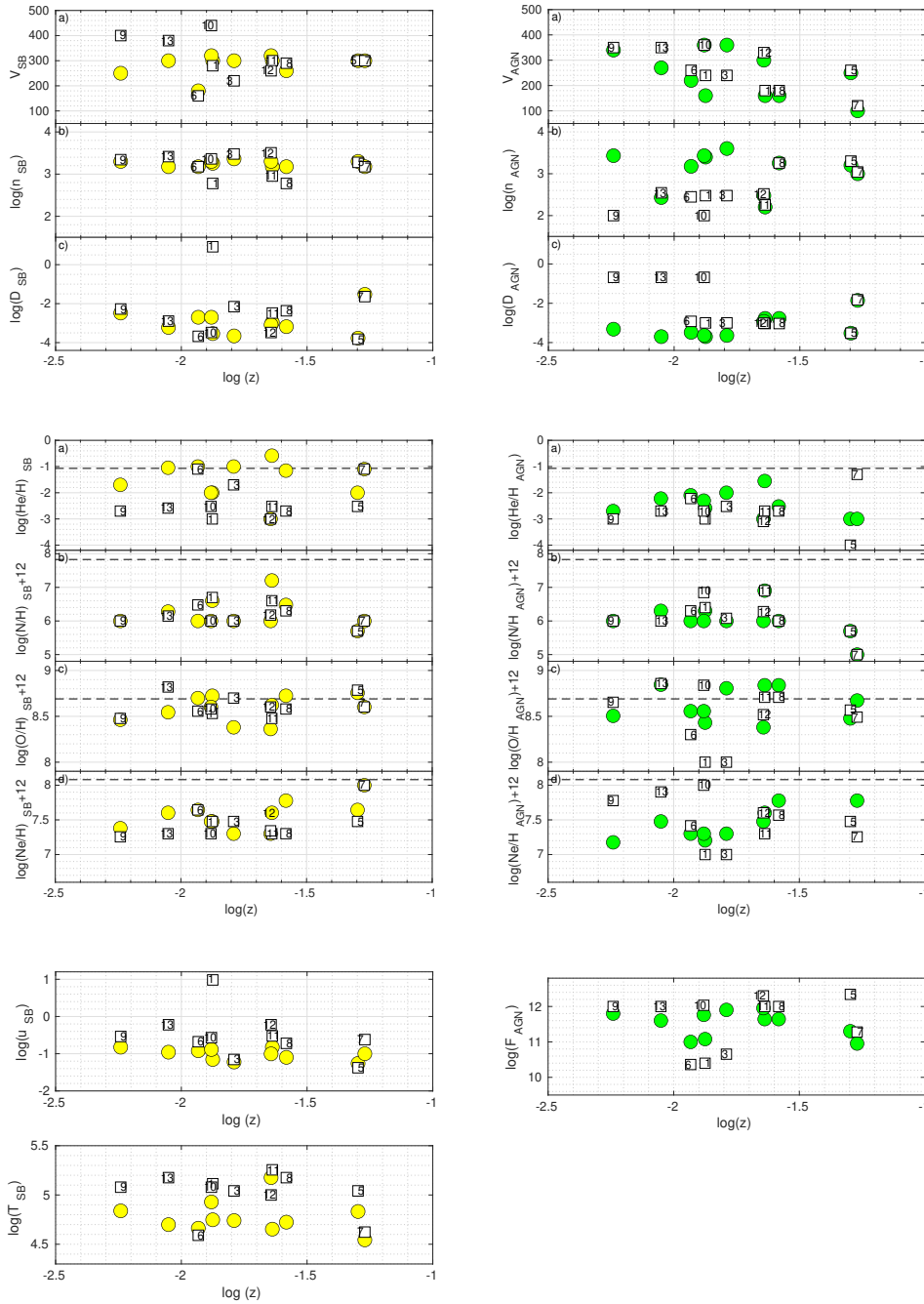


**Fig. 8.** Left. Distribution of the calculated physical parameters representing the shock (top panels), of the calculated element relative abundances (middle panels) and of the radiation parameters (bottom diagrams) as function of  $z$  for SB (left) and AGN models (right). Yellow circles: accretion, white squares: ejection. Right. The same for AGN models but green is for accretion and white for ejection. Dashed lines show the solar abundance ratios to H (Grevesse 2019).

### 3.4.2. [NII]/[OII]

In Fig. 10 [NII]/[OII] line ratios are shown as function of the redshift. [NII] and [OII] are linked by charge exchange reactions therefore increasing or decreasing trends depend at most on the N/O relative abundance. N5 and N7 do not appear in the diagrams because no data for [NII] were reported. N9 is an upper limit. We have added in Figs. 10 the N/O abundance ratios for each galaxy calculated by SB (right) and AGN models (left), respectively. Line intensity ratios are calculated by multiplying one term which depends on the collision strengths (and derives

from quantum mechanics), another term which depends on thermal equilibrium and a term which contains the relative abundances of the elements. If charge exchange reactions link the two lines, the result will be proportional in particular to the relative abundance of the elements. Therefore the [NII]/[OII] trend will follow the N/O trend. This can be roughly seen in Figure 10 panels, considering that for galaxy N9 the line ratio is an upper limit. To recover their values N/O ratios should be multiplied by the factor which depends on the collisional parameters of both lines and on the temperature of the emitting gas (Williams 1967). The sample is poor in number of galaxies and it covers a restricted

**Table 3.** Symbols in Figs. 11 and 12

symbol	object	Ref.
encircled dot	SLSNR hosts	(1)
triangles at $z \geq 0.1$	SLSNII hosts	(2)
filled triangles	SLSNI hosts	(3)
square+dot	only shock models for SLSN hosts	(4)
square+cross	Type Ic host central	(5)
circle+cross	Type Ic host at SN positions	(6)
triangles at $z \leq 0.1$	SN Ib host	(7)
encircled triangles	SN Iib hosts	(8)
opposite triangles	SN Ic hosts	(9)
double triangles	SN IcBL hosts	(10)
hexagrams	SN Ibc	(11)
asterisks	GRB hosts	(12)
triangle+cross	LGRB hosts	(13)
pentagrams	LGRB different hosts	(14)
triangle +plus	LGRB hosts with WR stars	(15)
encircled asterisks	LGRB at low z	(16)
hexagrams	SGRB hosts	(17)
dots	starburst galaxies	(19,25)
green open circles	AGN	(20,21,25)
filled circles	LINER	(22)
plus	low-luminosity nearby galaxies	(23)
cross	HII regions in local galaxies	(24)
green open circles	AGN	(27)

(1), (2), (3), (4) (Leloudas et al 2015); (5), (6) (Modjaz et al 2008); (7), (8), (9), (10), (11) (Sanders et al 2012); (12) (Krühler et al 2015); (13) (Savaglio et al 2009); (14) (Contini 2016a, table 8); (15) (Han et al 2010); (16) (Niino et al 2016); (17) (de Ugarte Postigo et al 2014); (19), (20) (Contini 2014); (21) (Koski 1978, Cohen 1983, Kraemer et al 1994, Dopita et al 2015); (22) (Contini 1997); (23) (Marino et al 2013); (24) (Berg et al 2012); (25) (Contini 2016b); (27) (Dors et al 2021);

This table is updated from Contini (2017, Table 9).

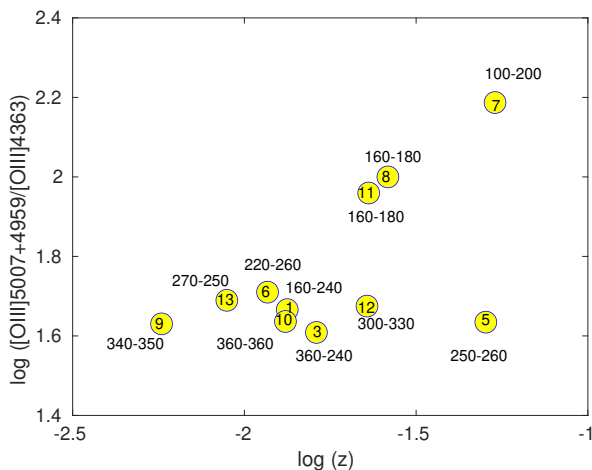


**Fig. 9.** Observed  $[OIII]5007+4959/[OII]4363$  vs redshift (yellow filled circles). Numbers refer to the shock velocities calculated by the models in  $\text{km s}^{-1}$  presented in Appendix A

redshift range which is less adapted to extrapolate to higher z. Alternatively, the different trends could be interpreted as simple fluctuations.

### 3.4.3. N/O abundance ratios and bursting-stars formation

Figs. 11 and 12 are updated from Contini (2017, Figs. 6 and 7, respectively). In Fig. 11 we compare  $\log(N/O)$  as function of  $12+\log(O/H)$  for different SB galaxies (see Table 3, updated from Contini 2017, Table 9) accounting in particular for the present model results for Nakajima et al EMPGs and (Fig. 12) also for the rich sample of AGN presented by Dors et al (2021).

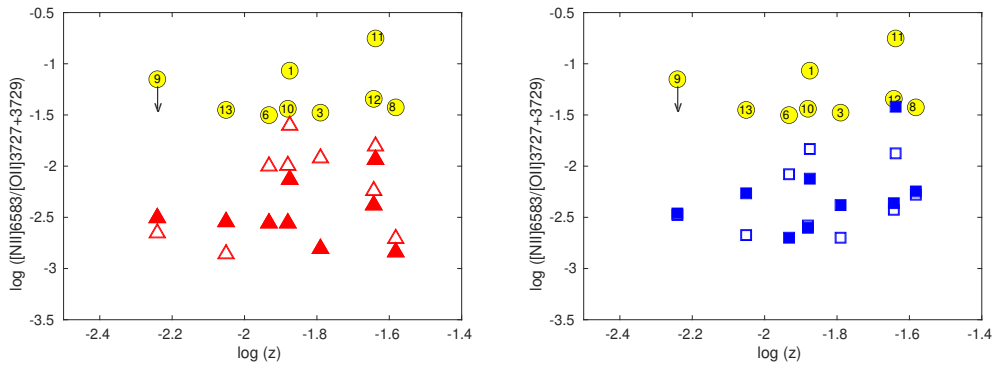
Although the Nakajima et al sample of EMPGs is not rich in number of objects, we have investigated the  $\log(N/O)$  trend as function of  $12+\log(O/H)$  of SB dominated galaxy model results in Fig. 11. First we have shifted our results multiplying N/O (large blue squares, filled for accretion and open for ejection) by a factor of 10. In this way EMPGs cover the region between GRB host galaxies and super-luminous SN hosts. Henry, Edmunds & Koppen (2000) claim that intermediate-mass stars between 4 and 8  $M_{\odot}$  dominate nitrogen production while massive stars dominate oxygen production. Nitrogen is primary at low metallicity but when  $12+\log(O/H) > 8.3$  secondary N becomes prominent. At  $12+\log(O/H) \sim 8.25$   $\log(N/O)$  turns upwards and rises steeply. For Mouhcine & Contini (2002) it turns upwards steeply at 8.7, similarly to our results for EMPGs which turn up steeply at  $\sim 8.7$ . This happens because nitrogen synthesis in intermediate mass stars is increasing with metallicity while oxygen production in massive stars is decreasing. However, at  $12+\log(O/H) > 8.3$   $\log(N/O)$  calculated by our models for EMPGs slightly decreases towards  $12+\log(O/H)=8.7$ , opposite to Henry et al fig. 1b and Mouhcine & Contini Fig. 1 trends. Mouhcine & Contini, in particular, claim that "for bursting-star formation, the observed dispersion in the N/O vs O/H relation is explained by the time delay between the release of oxygen by massive stars into the ISM and that of nitrogen by intermediate-mass stars. During the starburst event, as massive stars dominate the chemical enrichment, the galaxy moves towards the lower right part of the diagram in their Fig. 1. After the end of the burst nitrogen increases at constant oxygen."

Fig. 11 shows that N/O ratios calculated for EMPGs are lower by a factor of  $\sim 10$  than those calculated for other galaxies with the same metallicity. Mouhcine et & Contini suggest that "the low N/O abundance ratio with respect to other galaxies with comparable metallicities is well explained if they have just undergone a powerful starburst which have enriched their ISM in oxygen. In these objects nitrogen may have not been completely released."

We would like to explore how the N/O trend develops with the redshift. In Fig. 12 the  $\log(N/O)$  ratio calculated for the Nakajima et al sample is compared with different galaxy types described in Table 3. As well as for Fig. 11, they were selected on the basis that the parameters were calculated by the same code. At present we can roughly recognise a peak for LINERs at  $z \sim 0.006$ , a rather poor peak for SB galaxies at  $z \sim 1.0$  and a double maximum for SB accretion and AGN ejection models at  $z \sim 0.012$  for EMPG models. Fig. 12 confirms that EMPGs are extremely nitrogen-poor objects.

## 4. Concluding remarks

The galaxy sample presented by Nakajima et al. (2022) between  $z=0.00574$  and  $z=0.05045$  was selected because of oxygen deficiency. We have modelled the spectra by the *SUMA* code which accounts for both photoionization and shocks because it can be used to distinguish between accretion towards and ejection of matter from the radiation source. The detailed analysis of the line ratios presented in the first sections shows that the EMPGs in



**Fig. 10.** Observed  $[NII]6583/[OII]3727+3729$  vs redshift (yellow filled circles). We have added in Fig. 10 left panel the calculated  $\log(N/O)$  as function of  $z$  for AGN models (red triangles) and in the right panel the calculated  $\log(N/O)$  as function of  $z$  for SB models (blue squares). Filled is for accretion and open is for ejection. The Y-axis scale is the same for all the ratios. (see sect. 3.4.2, first paragraph).

**Table 4.** Comparison of oxygen metallicity

galaxy	$12+\log(O/H)^1$	$12+\log(O/H)_0^2$	$12+\log(O/H)_1^3$	$12+\log(O/H)_0^4$	$12+\log(O/H)_1^5$
HSC J0845+0131 (N1)	7.35	8.43	8.0	8.72	8
HSC J0935-0115 (N3)	7.17	8.8	8.0	8.38	8.7
HSC J1237-0016 (N5)	7.55	8.48	8.57	8.75	8.56
HSC J1401-0040 (N6)	7.64	8.55	8.3	8.7	8.3
HSC J1407-0047 (N7)	–	8.67	8.49	8.6	8.49
HSC J1411-0032 (N8)	8.12	8.84	8.7	8.72	8.7
HSC J1452+0241 (N9)	7.2	8.5	8.65	8.46	8.65
SDSS J1044+0353 (N10)	7.45	8.55	8.84	8.6	8.84
SDSS J1253-0312 (N11)	8.09	8.84	8.7	8.62	8.16
SDSS J1323-0312 (N12)	7.74	8.38	8.52	8.36	8.5
SDSS J1418+2102 (N13)	7.64	8.84	8.86	8.54	8.36

<sup>1</sup> calculated by Nakajima et al.; <sup>2</sup> calculated by models mh1-mh13 (str=0); <sup>3</sup> calculated by models mh1-mh13 (str=1); <sup>4</sup> calculated by models ms1-ms13 (str=0); <sup>5</sup> calculated by models ms1-ms13 (str=1)

the Nakajima et al sample have various element abundances and morphologies. We have adopted in this paper the updated solar  $\log(O/H)+12=8.69$  by Grevesse (2019). Then, in Fig. 11 a few SB dominated EMPGs show near-solar O/H abundance ratios, and a few AGN dominated models show O/H even higher than solar (see Fig.8), which is in agreement with AGN in general. Our results demonstrate that low oxygen line ratios to  $H\beta$  not always indicate a proportional O/H relative deficiency, such as to justify their classification as EMPG. Table 4 shows that the oxygen metallicities calculated by our models are higher than those calculated by the strong line method. On the other hand N/H ratios reach values lower than  $(N/H)_\odot$  by factors  $\sim 135$ . Therefore, our results justify the classification of the Nakajima et al sample among EMPG if nitrogen is also included among the "extremely poor metals". He/H are depleted by factors between 10 and 100 when AGN models are adopted as well as for SB models in the ejection case. SB accreting models show about solar He/H abundances ratios which indicate that accreted matter is coming from the ISM. We suggest a classification of the Nakajima et al sample objects selecting the models which best reproduce the spectra. All the SDSS objects and HSC N8 galaxy can be interpreted as merging products on the basis of a composite AGN + SB nature.

In the second part of the paper, although the Nakajima et al sample of EMPGs is not rich in number of objects, we have discussed the  $\log(N/O)$  trend as function of  $12+\log(O/H)$  and of the redshift. Bursting-star trends are confirmed as well as strong metal deficiency, in particular, of nitrogen. The N/O trend as

function of the redshift gives only a hint for the AGN-LINER and SB peak locations in general.

## References

- Aldrovandi, S.M.V. & Contini, M. 1985 A&A, 149, 109  
Asplund, M., Grevesse, N., Sauval, A. J., Scott, P. 2009, ARA&A, 47,481  
Baldwin, J.A., Phillips, M.M., Terlevich, R. 1981, PASP, 93,5  
Berg, D.A. et al 2012, ApJ, 754, 98  
Berg, D.A., Skillman, E.D., Henry, R.B.C., Erb, D.K., Carigi, L. 2016, ApJ, 826, 21  
Cohen, R.D. 1983, ApJ, 273, 489  
Contini, M., Aldrovandi, S.M.V. 1983, A&A, 127, 15  
Contini, M. 1997, A&A, 323, 71  
Contini, M., Viegas, S.M. 2001, ApJS, 132, 211  
Contini, M., Viegas, S.M. 2001, ApJS, 137, 75  
Contini, M. 2012, MNRAS, 426, 719  
Contini, M. 2013, MNRAS, 429, 242  
Contini, M. 2014, A&A, 564, 19  
Contini, M. 2016a, MNRAS, 460, 3232  
Contini, M. 2016b, MNRAS, 461, 2374  
Contini, M. 2017, MNRAS, 469, 3125  
Contini, M. 2022 arXiv:2201.06004  
Cox, D.P. 1972, ApJ, 178, 1159  
de Ugarte Postigo, A. et al 2014, A&A, 563, 62  
Dittmann, A.J., Cantiello, M., Jermin, A.J. 2021, ApJ, 916, 48  
Do, T. et al 2018, ApJL, 855, L5  
Dopita, M.M. et al. 2015, ApJS, 217, 12  
Dors, O.L., Contini, M., Riffel, R.A., Pérez-Montero, E., Krabbe, A.C., Cardaci, M.V., Hägele, G.F. 2021, MNRAS, 501, 1370  
Erb, D.K., Pettini, M., Shapley, A.E. et al. 2010, ApJ, 719, 1168  
Fonseca-Faria, M.A., Rodríguez-Ardila, A., Contini, M., Dahmer-Hahn, L.G., Morganti, R. 2023, MNRAS, 524,143

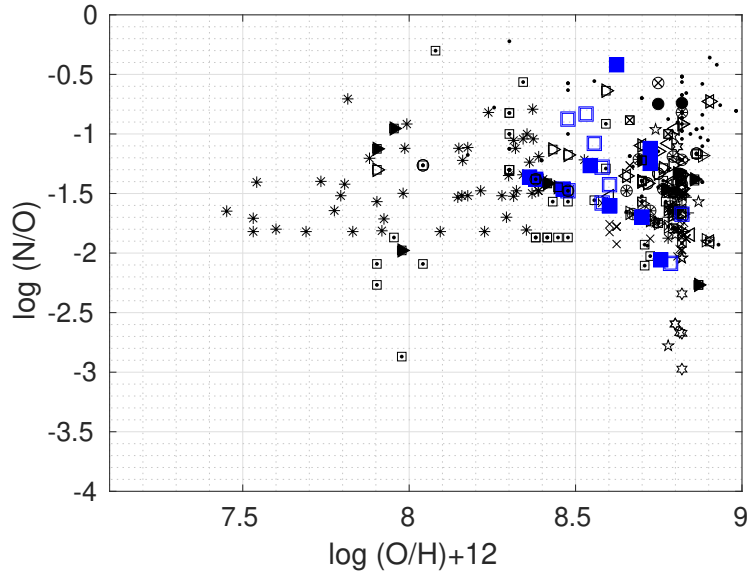


**Fig. 11.** N/O relative abundances as function of  $12+\log(\text{O}/\text{H})$  calculated in this paper by SB models (blue squares). Open is for ejection, filled for accretion. The calculated N/O ratios are shifted towards higher values by a factor of 10. Symbols for the other galaxy types are explained in Table 3.

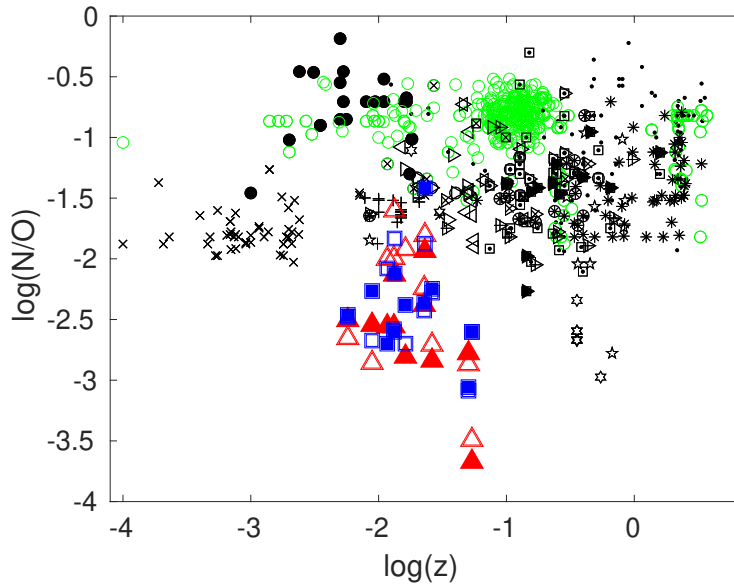


**Fig. 12.** N/O relative abundances as function of  $\log(z)$  calculated in this paper. Symbols as in Fig. 11.

- Ginolfi, M., et al 2020, *A&A*, 633, A90  
 Goldman, I. 2024, arXiv:2406.08578  
 Goldman, I. & Fleck, R. 2023, *MNRAS*, 521, 2949  
 Grevesse, N. 2019 in *The Solar Chemical Composition: Past and Present*, Bulletin de la Société Royale des Sciences de Liège [En ligne], Volume 88 - Année 2019  
 Han, X.H., Hammer, F., Liang, Y. C., Flores, H., Rodrigues, M., Hou, J. L., Wei, J. Y. 2010, *A&A*, 514, 24  
 Hayden-Pawson, E. et al 2021 arXiv:2110.00033  
 Henry, R.B.C., Edmunds, M.G. & Köppen, J. 2000, *ApJ*, 541, 660  
 Hunger, V.K., Groote, D. 1999, *A&A*, 351, 554  
 Isobe, Y. et al 2015, *MNRAS*, 451, 93  
 Izotov, Y.I., Guseva, N.G., Fricke, K.J., Henkel, C., Schaerer, D., Thuan, T.X. 2021, *A&A*, 646, 138  
 Kauffmann, G. et al. 2003, *MNRAS*, 341, 33  
 Kewley, L.J., Dopita, M.A., Sutherland, R.S., Heisler, C.A., Trevena, J. 2001, *ApJ*, 556, 121  
 Kewley, L.J. & Dopita, M.A. 2002, *ApJS*, 142, 35  
 Kojima, K. et al 2020, *ApJ*, 898, 142  
 Koski, A. 1978, *ApJ*, 223, 56  
 Kraemer, S.B., Wu, C.-C., Crenshaw, D.M., Harrington, J.P. 1994, *ApJ*, 435, 171  
 Krühler, T. et al 2015, *A&A*, 581, 125  
 Leloudas, G. et al 2015, *MNRAS*, 574, A61  
 Marino, R.A. et al. 2013, *A&A*, 559, 114  
 Meshkov, E.E. 1969, *FIDy*, 4(5), 101  
 Modjaz, M. et al 2008, *AJ*, 135, 1136  
 Morganti, R. 2023, *MNRAS*, 524, 143  
 Mouhcine, M. & Contini, T. 2002, *A&A*, 389, 106  
 Murray, N. & Chiang, T. 1997, *ApJ*, 474, 91  
 Nakajima, K., Ouchi, M., Xu, Y., et al 2022, *ApJS*, 262, 3  
 Niino, Y. et al 2016, *LPI Contrib*, 1962, 4039  
 Osterbrock, D.E. 1974 in *Astrophysics of Gaseous Nebulae*, San Francisco, W.H. Freeman and Co., 1974  
 Rigby, J.R. & Rieke, G.H. 2004, *ApJ*, 606, 237  
 Sancisi, R., Fraternali, F., Oosterloo, T., van der Hulst, T. 2008, *A&ARv*, 15, 189S

- Sanders, N.E. et al. 2012, ApJ, 758, 132  
Savaglio, S., Glazerbrook, K., Le Borgne, D. 2009, ApJ, 691, 182  
Shaerer, D. 2002, A&A, 382, 28  
Shaerer, D. 2003, A&A, 397, 527  
Shaerer, D., Fragos, T., Izotov, Y.I. 2019, A&A, 622, L10  
Umeda, H., 2022, ApJ, 930, 37  
Yu, B.P.B., Owen, E.R., Pan, K.-C., Wu, K., Ferreras, I. 2021, arXiv:2109.09764  
Young, P.R. 2018, ApJ, 855, 15  
Vanzella, E. et al 2023, A&A, 678, A473  
Viegas, S.M., Contini, M. 1994, ApJ, 428, 113  
Zhang, Y. et al 2023, arXiv:2306.07940  
Zhang, Y. et al 2017, MNRAS, 466, 3217

## Appendix A: Tables

**Table A.1.** Comparison of observed with calculated line ratios to  $H\beta=1$  for the Nakajima et al. galaxies

HSC	N1	mp1.0	mp1.1	N3	mp3.0	mp3.1	N5	mp5.0	mp5.1	N6	mp6.0	mp6.1
[OII]3727+	0.42	0.36	0.37	0.21	0.23	0.26	0.43	0.39	0.42	0.825	0.72	0.7
[NeIII]3896+	0.29	0.31	0.31	0.25	0.3	0.27	0.71	0.75	0.84	0.42	0.34	0.4
H $\gamma$ 4340	0.443	0.46	0.44	0.445	0.46	0.45	0.49	0.46	0.46	0.5	0.46	0.45
[OIII]4363	0.085	0.07	0.05	0.08	0.05	0.036	0.167	0.125	0.08	0.124	0.083	0.45
HeII 4686	<0.01	0.9	0.09	0.024	0.06	0.18	<0.0128	0.19	0.22	0.03	0.12	0.12
H $\beta$ 4861	1	1	1	1	1	1	1	1	1	1	1	1
[OIII]5007+	3.94	4.0	4.3	3.25	3.25	3.0	7.2	7.5	7.0	6.36	7.0	5.9
HeI 5876	0.21	0.21	0.12	0.086	0.13	0.1	0.13	0.11	0.126	0.094	0.1	0.08
H $\alpha$ 6563	2.67	2.9	3.6	2.53	2.9	3.16	2.84	2.9	3.0	2.87	2.9	3.15
[NII]6583	0.036	0.037	0.03	0.007	0.007	0.009	-	0.007	0.007	0.026	0.04	0.04
[SII]6716	0.04	0.03	0.016	0.023	0.02	0.016	0.032	0.024	0.18	0.089	0.044	0.24
[SII]6730	0.02	0.07	0.033	0.01	0.04	0.036	0.03	0.054	0.39	0.06	0.1	0.49
H $\beta_{calc}$ <sup>0</sup>	-	6.7	4.24	-	7.7	3.75	-	2.3	2.2	-	1.6	1.5
$V_s$ <sup>1</sup>	-	200	200	-	300	300	-	250	300	-	180	180
$n_0$ <sup>2</sup>	-	2000	2000	-	2000	2000	-	2000	2000	-	1800	1800
$D$ <sup>3</sup>	-	0.0176	0.83	-	0.007	0.007	-	0.0037	0.0025	-	0.007	0.007
$F$ <sup>4</sup>	-	9e11	9e11	-	9e11	8e11	-	8.6e11	9e11	-	4.2e11	4.2e11
He/H	-	0.16	0.1	-	0.1	0.1	-	0.09	0.09	-	0.08	0.08
N/H <sup>5</sup>	-	0.04	0.04	-	0.01	0.01	-	0.005	0.005	-	0.03	0.03
O/H <sup>5</sup>	-	7.0	7	-	6.6	5.6	-	4.6	5.6	-	7.8	7.8
Ne/H <sup>5</sup>	-	0.6	0.5	-	0.6	0.3	-	0.5	0.5	-	0.4	0.4
S/H <sup>5</sup>	-	0.2	0.02	-	0.2	0.03	-	0.2	0.2	-	0.2	0.2
str	-	0	1	-	0	1	-	0	1	-	0	1

<sup>0</sup> erg cm<sup>-2</sup> s<sup>-1</sup>; <sup>1</sup> km s<sup>-1</sup>; <sup>2</sup> cm<sup>-3</sup>; <sup>3</sup> parsec; <sup>4</sup> photon cm<sup>-2</sup> s<sup>-1</sup> eV<sup>-1</sup> at the Lyman limit; <sup>5</sup> in 10<sup>-4</sup> units

**Table A.2.** Comparison of observed with calculated line ratios to  $H\beta=1$  for the Nakajima et al. galaxies

HSC	N7	mp7.0	mp7.1	N8	mp8.0	mp8.1	N9	mp9.0	mp9.1
[OII]3727+	0.82	0.74	0.7	0.8	1.0	1.0	0.17	0.23	0.19
[NeIII]3896+	0.34	0.3	0.4	0.74	0.87	1.0	0.23	0.27	0.35
H $\gamma$ 4340	0.47	0.46	0.45	0.53	0.46	0.46	0.46	0.46	0.45
[OIII]4363	<0.026	0.06	0.037	0.10	0.13	0.1	0.078	0.05	0.026
HeII4686	-	0.12	0.13	-	0.19	0.23	<0.013	0.068	0.813
H $\beta$ 4861	1	1	1	1	1	1	1	1	1
[OIII]5007+	4.0	4.6	4.0	10.0	10.5	11.9	3.23	3.24	2.2
HeI 5876	0.092	0.11	0.13	0.106	0.12	0.12	0.13	0.13	0.11
H $\alpha$ 6563	2.78	2.9	3.12	3.0	2.9	2.98	2.83	2.9	3.1
[NII]6583	-	0.02	0.02	0.03	0.02	0.02	<0.012	0.007	0.007
[SII]6716	0.094	0.11	0.096	-	0.06	0.15	0.016	0.011	0.04
[SII]6730	0.1	0.24	0.2	0.05	0.13	0.25	0.013	0.02	0.09
H $\beta_{calc}$ <sup>0</sup>	-	2.1	1	-	1.27	0.94	-	7.8	4.4
$V_s$ <sup>1</sup>	-	180	210	-	160	160	-	300	300
$n_0$ <sup>2</sup>	-	1500	1500	-	1800	1800	-	2000	2000
$D$ <sup>3</sup>	-	0.03	0.013	-	0.0017	0.0017	-	0.007	0.0077
$F$ <sup>4</sup>	-	4.2e11	4.2e11	-	4.4e11	4.4e11	-	9e11	9e11
He/H	-	0.1	0.1	-	0.1	0.1	-	0.1	0.1
N/H <sup>5</sup>	-	0.01	0.01	-	0.01	0.01	-	0.01	0.01
O/H <sup>5</sup>	-	4.6	4.6	-	6.9	6.9	-	6.2	5.2
Ne/H <sup>5</sup>	-	0.3	0.3	-	0.6	0.6	-	0.5	0.5
S/H <sup>5</sup>	-	0.2	0.2	-	0.1	0.09	-	0.1	0.1
str	-	0	1	-	0	1	-	0	1

<sup>0</sup> erg cm<sup>-2</sup> s<sup>-1</sup>; <sup>1</sup> km s<sup>-1</sup>; <sup>2</sup> cm<sup>-3</sup>; <sup>3</sup> parsec; <sup>4</sup> photon cm<sup>-2</sup> s<sup>-1</sup> eV<sup>-1</sup> at the Lyman limit; <sup>5</sup> in 10<sup>-4</sup> units

**Table A.3.** Comparison of observed with calculated line ratios to  $H\beta=1$  for the Nakajima et al. galaxies

HSC	N1	mh1.0	mh1.1	N3	mh3.0	mh3.1	N5	mh5.0	mh5.1	N6	mh6.0	mh6.1
[OII]3727+	0.42	0.5	0.47	0.21	0.20	0.21	0.43	0.44	0.45	0.825	0.85	0.83
[NeIII]3896+	0.29	0.32	0.22	0.25	0.28	0.2	0.71	0.71	0.73	0.42	0.41	0.45
H $\gamma$ 4340	0.443	0.46	0.46	0.445	0.46	0.46	0.49	0.46	0.46	0.5	0.464	0.46
[OIII]4363	0.085	0.10	0.085	0.08	0.082	0.076	0.167	0.16	0.18	0.124	0.137	0.10
HeII 4686	<0.01	0.008	0.005	0.024	0.027	0.021	<0.0128	0.004	0.018	0.03	0.025	0.03
H $\beta$ 4861	1	1	1	1	1	1	1	1	1	1	1	1
[OIII]5007+	3.94	3.89	4.0	3.25	3.1	4.17	7.2	8.46	7.66	6.36	6.0	6.29
HeI 5876	0.21	0.003	0.001	0.086	0.012	0.02	0.13	0.001	0.001	0.094	0.009	0.005
H $\alpha$ 6563	2.67	2.92	2.97	2.53	2.89	2.95	2.9	2.9	3.2	2.87	2.92	2.94
[NII]6583	0.036	0.032	0.04	0.007	0.006	0.007	-	0.007	0.007	0.026	0.021	0.027
[SII]6716	0.04	0.034	0.015	0.023	0.01	0.012	0.032	0.02	0.03	0.089	0.031	0.03
[SII]6730	0.02	0.079	0.03	0.01	0.023	0.03	0.03	0.048	0.07	0.06	0.071	0.06
H $\beta_{calc}$ <sup>0</sup>	-	0.068	0.005	-	1.8	0.005	-	2	3	-	0.05	0.007
V <sub>s</sub> <sup>1</sup>	-	160	240	-	360	240	-	250	260	-	220	260
n <sub>0</sub> <sup>2</sup>	-	2500	300	-	4000	300	-	1600	2000	-	1500	280
D <sup>3</sup>	-	2.e-4	1e-3	-	2.3e-4	0.001	-	3.e-4	3.e-4	-	3.3e-4	1.2e-3
F <sup>4</sup>	-	1.2e11	2.5e10	-	8e11	4.5e10	-	2.0e11	2.2e12	-	1.0e11	2.3e10
He/H	-	0.0026	0.001	-	0.01	0.003	-	0.001	-	-	0.008	0.006
N/H <sup>5</sup>	-	0.02	0.025	-	0.01	0.012	-	0.007	-	-	0.01	0.02
O/H <sup>5</sup>	-	2.7	1	-	6.4	1.0	-	3.0	3.7	-	3.6	2
Ne/H <sup>5</sup>	-	0.16	0.1	-	0.2	0.1	-	0.03	0.3	-	0.2	0.26
S/H <sup>5</sup>	-	0.2	0.03	-	0.2	0.06	-	0.2	0.15	-	0.15	0.06
str	-	0	1	-	0	1	-	0	1	-	0	1

<sup>0</sup> erg cm<sup>-2</sup> s<sup>-1</sup>; <sup>1</sup> km s<sup>-1</sup>; <sup>2</sup> cm<sup>-3</sup>; <sup>3</sup> parsec; <sup>4</sup> photon cm<sup>-2</sup> s<sup>-1</sup> eV<sup>-1</sup> at the Lyman limit; <sup>5</sup> in 10<sup>-4</sup> units

**Table A.4.** Comparison of observed with calculated line ratios to  $H\beta=1$  for the Nakajima et al. galaxies

HSC	N7	mh7.0	mh7.1	N8	mh8.0	mh8.1	N9	mh9.0	mh9.1
[OII]3727+	0.82	0.82	0.84	0.8	0.88	0.9	0.17	0.19	0.18
[NeIII]3896+	0.34	0.32	0.45	0.74	0.74	0.81	0.23	0.27	0.26
H $\gamma$ 4340	0.47	0.46	0.46	0.53	0.46	0.46	0.46	0.46	0.40
[OIII]4363	<0.026	0.026	0.029	0.10	0.09	0.09	0.078	0.07	0.071
HeII4686	-	0.004	0.16	-	0.018	0.018	<0.013	0.008	0.0085
H $\beta$ 4861	1	1	1	1	1	1	1	1	1
[OIII]5007+	4.0	3.2	3.6	10.0	9.5	10.14	3.33	3.68	3.5
HeI 5876	0.092	0.001	0.074	0.106	0.002	0.001	0.13	2.1e-3	1.e-5
H $\alpha$ 6563	2.78	2.9	3.1	3.0	2.9	3.14	2.83	2.9	4.5
[NII]6583	-	0.015	0.01	0.03	0.02	0.02	<0.012	0.009	0.002
[SII]6716	0.094	0.06	0.12	-	0.05	0.04	0.016	0.01	0.0016
[SII]6730	0.1	0.13	0.23	0.05	0.1	0.09	0.013	0.017	0.0023
H $\beta_{calc}$ <sup>0</sup>	-	0.56	0.51	-	1.36	1.75	-	1.27	0.37
V <sub>s</sub> <sup>1</sup>	-	100	200	-	160	180	-	340	350
n <sub>0</sub> <sup>2</sup>	-	1000	1100	-	1800	1800	-	2700	100
D <sup>3</sup>	-	0.014	0.015	-	0.0017	9.3e-4	-	4.8e-4	0.21
F <sup>4</sup>	-	9.0e10	1.9e11	-	4.4e11	1.e12	-	6.3e11	1e12
He/H	-	0.001	0.05	-	0.003	0.002	-	0.002	0.001
N/H <sup>5</sup>	-	0.01	0.005	-	0.01	0.01	-	0.01	0.01
O/H <sup>5</sup>	-	4.7	3.1	-	6.9	5.1	-	3.2	4.5
Ne/H <sup>5</sup>	-	0.6	0.18	-	0.6	0.37	-	0.15	0.6
S/H <sup>5</sup>	-	0.1	0.04	-	0.2	0.1	-	0.1	0.3
str	-	0	1	-	0	1	-	0	1

<sup>0</sup> erg cm<sup>-2</sup> s<sup>-1</sup>; <sup>1</sup> km s<sup>-1</sup>; <sup>2</sup> cm<sup>-3</sup>; <sup>3</sup> parsec; <sup>4</sup> photon cm<sup>-2</sup> s<sup>-1</sup> eV<sup>-1</sup> at the Lyman limit; <sup>5</sup> in 10<sup>-4</sup> units

**Table A.5.** Comparison of observed with calculated line ratios to  $H\beta=1$  for the Nakajima et al. galaxies

SDSS	N10	mh10.0	mh10.1	N11	mh11.0	mh11.1	N12	mh12.0	mh12.1	N13	mh13.0	mh13.1
[OII]3727+	0.22	0.22	0.28	0.849	0.90	0.90	0.176	0.17	0.17	0.48	0.45	0.49
[NeIII]3896+	0.42	0.44	0.44	0.52	0.52	0.5	0.73	0.89	0.75	0.517	0.51	0.43
H $\gamma$ 4340	0.48	0.47	0.40	0.49	0.464	0.46	0.49	0.47	0.47	0.48	0.46	0.40
[OIII]4363	0.134	0.133	0.112	0.11	0.09	0.093	0.22	0.19	0.16	0.149	0.145	0.14
HeII 4686	0.018	0.02	0.017	0.017	0.018	0.016	0.008	0.008	0.008	0.022	0.021	0.017
H $\beta$ 4861	1	1	1	1	1	1	1	1	1	1	1	1
[OIII]5007+	5.8	5.9	5.5	10.02	9.8	10.6	10.41	10.88	11.6	7.29	7.5	7.2
HeI 5876	0.086	0.005	2.3e-5	0.11	0.002	0.001	0.097	6.e-4	1.6e-4	0.101	0.007	1.2e-5
H $\alpha$ 6563	2.65	2.89	4.5	2.74	2.89	3.14	2.88	2.87	2.9	2.84	2.9	4.5
[NII]6583	0.008	0.008	0.009	0.15	0.14	0.18	0.008	0.009	0.009	0.017	0.018	0.018
[SII]6716	0.02	0.005	0.002	0.072	0.05	0.04	-	9e-4	6.4e-4	0.046	0.01	2.9e-3
[SII]6730	0.016	0.012	0.0026	0.073	0.1	0.09	-	0.002	0.0015	0.031	0.03	4.2e-3
H $\beta$ <sub>calc</sub> <sup>0</sup>	-	0.43	0.39	-	1.33	1.78	-	0.71	1.55	-	0.34	0.37
V <sub>s</sub> <sup>1</sup>	-	360	360	-	160	180	-	300	330	-	270	350
n <sub>0</sub> <sup>2</sup>	-	2700	100	-	1800	1800	-	1800	1100	-	3000	100
D <sup>3</sup>	-	2.3e-4	0.21	-	0.0017	9.3e-4	-	0.0012	9.7e-4	-	2.e-4	0.21
F <sup>4</sup>	-	5.8e11	1.08e12	-	4.4e11	1.e12	-	9e11	2e12	-	4e11	1e12
He/H	-	0.005	0.002	-	0.028	0.002	-	0.001	0.0008	-	0.006	0.002
N/H <sup>5</sup>	-	0.01	0.07	-	0.08	0.08	-	0.01	0.019	-	0.02	0.01
O/H <sup>5</sup>	-	3.6	6.9	-	6.9	5.1	-	2.4	3.3	-	7.0	7.2
Ne/H <sup>5</sup>	-	0.2	1.0	-	0.4	0.2	-	0.3	0.4	-	0.3	0.8
S/H <sup>5</sup>	-	0.1	0.3	-	0.2	0.1	-	0.02	0.02	-	0.2	0.3
str	-	0	1	-	0	1	-	0	1	-	0	1

<sup>0</sup> erg cm<sup>-2</sup> s<sup>-1</sup>; <sup>1</sup> km s<sup>-1</sup>; <sup>2</sup> cm<sup>-3</sup>; <sup>3</sup> parsec; <sup>4</sup> photon cm<sup>-2</sup> s<sup>-1</sup> eV<sup>-1</sup> at the Lyman limit; <sup>5</sup> in 10<sup>-4</sup> units

**Table A.6.** Comparison of observed with calculated line ratios to  $H\beta=1$  for the Nakajima et al. galaxies

HSC	N1	ms1.0	ms1.1	N3	ms3.0	ms3.1	N5	ms5.0	ms5.1**	N6	ms6.0**	ms6.1
[OII]3727+	0.42	0.4	0.45	0.21	0.25	0.24	0.43	0.414	0.55	0.825	0.84	0.86
[NeIII]3896+	0.29	0.24	0.3	0.25	0.29	0.27	0.71	0.69	0.70	0.42	0.34	0.37
H $\gamma$ 4340	0.443	0.46	0.44	0.445	0.46	0.46	0.45	0.46	0.45	0.5	0.46	0.46
[OIII]4363	0.085	0.074	0.06	0.08	0.1	0.056	0.167	0.21	0.12	0.124	0.08	0.09
HeII 4686	<0.01	0.005	0.01	0.024	0.02	0.05	<0.013	0.01	0.008	0.03	0.002*	0.024
H $\beta$ 4861	1	1	1	1	1	1	1	1	1	1	1	1
[OIII]5007+	3.94	3.72	3.8	3.25	3.42	3.2	7.2	7.04	7.7	6.36	6.5	6.99
HeI 5876	0.21	0.08	8e-5	0.086	0.16	0.014	0.113	0.015	0.004	0.094	0.15	1.25
H $\alpha$ 6563	2.67	2.9	3.5	2.53	2.9	3.3	2.84	2.9	2.9	2.9	2.89	2.88
[NII]6583	0.036	0.036	0.05	0.007	0.01	0.009	-	0.01	0.012	0.026	0.02	0.03
[SII]6716	0.04	0.01	0.01	0.023	0.01	0.01	0.032	0.01	0.02	0.089	0.02	0.014
[SII]6730	0.02	0.03	0.02	0.01	0.022	0.024	0.03	0.02	0.05	0.06	0.05	0.031
H $\beta$ <sub>calc</sub> <sup>0</sup>	-	0.26	17.0	-	0.1	3.0	-	0.09	0.28	-	0.45	0.064
V <sub>s</sub> <sup>1</sup>	-	300	280	-	300	220	-	300	300	-	180	160
n <sub>0</sub> <sup>2</sup>	-	1800	600	-	2300	3000	-	2000	1900	-	1500	1500
D <sup>3</sup>	-	2.9e-4	8.3	-	2.2e-4	0.007	-	1.7e-4	1.5e-4	-	2.e-3	2.1e-4
T <sub>*</sub> <sup>4</sup>	-	5.6	13.0	-	5.5	11.0	-	6.8	11.	-	4.6	3.9
U	-	0.07	9.6	-	0.06	0.07	-	0.055	0.042	-	0.12	0.21
He/H	-	0.01	0.001	-	0.1	0.02	-	0.01	0.003	-	0.1	0.8
N/H <sup>5</sup>	-	0.04	0.05	-	0.01	0.01	-	0.005	0.005	-	0.01	0.03
O/H <sup>5</sup>	-	5.3	3.4	-	2.4	5.0	-	5.7	6.1	-	5.0	3.6
Ne/H <sup>5</sup>	-	0.3	0.3	-	0.2	0.3	-	0.44	0.3	-	0.44	0.44
S/H <sup>5</sup>	-	0.3	0.02	-	0.2	0.03	-	0.2	0.2	-	0.2	0.2
str	-	0	1	-	0	1	-	0	1	-	0	1

<sup>0</sup> erg cm<sup>-2</sup> s<sup>-1</sup>; <sup>1</sup> km s<sup>-1</sup>; <sup>2</sup> cm<sup>-3</sup>; <sup>3</sup> parsec; <sup>4</sup> 10<sup>4</sup>K; <sup>5</sup> in 10<sup>-4</sup> units; \* the line can be blended with [FeIII]4702 with ratios to H $\beta$  0.06; \*\*: models calculated by B<sub>0</sub>=6×10<sup>-5</sup>Gauss.

**Table A.7.** Comparison of observed with calculated line ratios to  $H\beta=1$  for the Nakajima et al. galaxies

HSC	N7	ms7.0	ms7.1	N8	ms8.0	ms8.1	N9	ms9.0	ms9.1
[OII]3727+	0.82	1.0	0.83	0.8	0.82	1.1	0.17	0.164	0.18
[NeIII]3896+	0.34	0.3	0.4	0.74	0.78	0.6	0.23	0.28	0.35
H $\gamma$ 4340	0.47	0.46	0.46	0.53	0.46	0.45	0.46	0.46	0.46
[OIII]4363	<0.026	0.024	0.015	0.10	0.126	0.1	0.078	0.064	0.055
HeII4686	-	0.002	0.002	-	0.01	0.02	<0.013	0.007	0.015
H $\beta$ 4861	1	1	1	1	1	1	1	1	1
[OIII]5007+	4.0	4.4	3.9	10.0	9.9	9.0	3.33	4.1	3.5
HeI 5876	0.092	0.12	0.12	0.106	0.11	0.003	0.13	0.026	0.0012
H $\alpha$ 6563	2.78	2.9	2.9	3.0	2.9	3.3	2.83	2.9	3.11
[NII]6583	-	0.007	0.01	0.03	0.035	0.046	<0.012	0.007	0.01
[SII]6716	0.094	0.013	0.12	-	0.014	0.02	0.016	0.016	0.013
[SII]6730	0.1	0.027	0.25	0.05	0.031	0.05	0.013	0.04	0.031
H $\beta_{calc}$ <sup>0</sup>	-	3.2	0.50	-	0.156	1.34	-	2.28	5.9
V <sub>s</sub> <sup>1</sup>	-	300	300	-	260	290	-	250	400
n <sub>0</sub> <sup>2</sup>	-	1500	1500	-	1500	600	-	2000	2200
D <sup>3</sup>	-	0.03	0.023	-	6.6e-4	4.3e-3	-	3.2e-3	5.3e-3
T <sub>*</sub> <sup>4</sup>	-	3.5	4.2	-	5.3	15.	-	6.9	12
U	-	0.1	0.24	-	0.08	0.19	-	0.15	0.29
He/H	-	0.08	0.08	-	0.07	0.002	-	0.02	0.002
N/H <sup>5</sup>	-	0.01	0.01	-	0.03	0.02	-	0.01	0.01
O/H <sup>5</sup>	-	4.0	4.0	-	5.3	3.8	-	2.9	3.0
Ne/H <sup>5</sup>	-	1.0	1.0	-	0.6	0.2	-	0.24	0.18
S/H <sup>5</sup>	-	0.2	0.06	-	0.2	0.01	-	0.2	0.03
str	-	0	1	-	0	1	-	0	1

<sup>0</sup> erg cm<sup>-2</sup> s<sup>-1</sup>; <sup>1</sup> km s<sup>-1</sup>; <sup>2</sup> cm<sup>-3</sup>; <sup>3</sup> parsec; <sup>4</sup> 10<sup>4</sup>K; <sup>5</sup> in 10<sup>-4</sup> units

**Table A.8.** Comparison of observed with calculated line ratios to  $H\beta=1$  for the Nakajima et al. galaxies

SDSS	N10	ms10.0	ms10.1	N11	ms11.0	ms11.1	N12	ms12.0	ms12.1	N13	ms13.0	ms13.1
[OII]3727+	0.22	0.19	0.19	0.85	0.85	1.10	0.176	0.23	0.2	0.48	0.47	0.46
[NeIII]3896+	0.42	0.42	0.42	0.52	0.45	0.54	0.73	0.73	0.62	0.517	0.6	0.49
H $\gamma$ 4340	0.48	0.46	0.46	0.49	0.47	0.44	0.49	0.46	0.46	0.48	0.47	0.46
[OIII]4363	0.134	0.09	0.11	0.11	0.11	0.13	0.22	0.19	0.21	0.149	0.16	0.14
HeII 4686	0.018	0.02	0.02	0.017	0.014	0.03	0.008	0.008	0.009	0.022	0.02	0.022
H $\beta$ 4861	1	1	1	1	1	1	1	1	1	1	1	1
[OIII]5007+	5.8	6.38	5.7	10.02	9.0	9.14	10.41	9.45	9.9	7.29	8.3	7.7
HeI 5876	0.086	0.012	0.002	0.11	0.41	0.001	0.097	5.e-4	4.e-4	0.101	0.14	0.003
H $\alpha$ 6563	2.65	2.9	3.0	2.74	2.87	3.7	2.88	3.0	3.1	2.84	2.9	3.2
[NII]6583	0.008	0.007	0.008	0.15	0.2	0.14	0.008	0.013	0.01	0.017	0.017	0.018
[SII]6716	0.02	0.016	0.008	0.072	0.03	0.02	-	8e-3	3e-3	0.046	0.014	0.03
[SII]6730	0.016	0.037	0.019	0.077	0.07	0.06	-	0.02	7.5e-3	0.031	0.31	0.06
H $\beta_{calc}$ <sup>0</sup>	-	2.3	6.2	-	0.13	1.7	-	0.72	7.1	-	0.18	4.0
V <sub>s</sub> <sup>1</sup>	-	320	440	-	300	300	-	320	260	-	300	380
n <sub>0</sub> <sup>2</sup>	-	2000	2300	-	1500	900	-	2000	3200	-	1500	2600
D <sup>3</sup>	-	0.002	3.3e-4	-	1.1e-3	3.3e-3	-	8.3e-4	3.3e-4	-	6.e-4	1.27e-3
T <sub>*</sub> <sup>4</sup>	-	8.5	12	-	4.5	18.0	-	15.0	10.0	-	5.0	15.0
U	-	0.13	0.27	-	0.15	0.3	-	0.099	0.6	-	0.1	0.16
He/H	-	0.01	0.003	-	0.26	0.003	-	0.001	0.001	-	0.09	0.0026
N/H <sup>5</sup>	-	0.01	0.01	-	0.16	0.04	-	0.01	0.015	-	0.019	0.014
O/H <sup>5</sup>	-	4.0	3.8	-	4.2	3.0	-	2.3	4.0	-	3.5	6.60
Ne/H <sup>5</sup>	-	0.3	0.2	-	0.4	0.16	-	0.2	0.22	-	0.4	0.2
S/H <sup>5</sup>	-	0.2	0.03	-	0.5	0.01	-	0.1	0.01	-	0.3	0.05
str	-	0	1	-	0	1	-	0	1	-	0	1

<sup>0</sup> erg cm<sup>-2</sup> s<sup>-1</sup>; <sup>1</sup> km s<sup>-1</sup>; <sup>2</sup> cm<sup>-3</sup>; <sup>3</sup> parsec; <sup>4</sup> 10<sup>4</sup>K; <sup>5</sup> in 10<sup>-4</sup> units